RWTH Aachen University

The Critical Casimir Force in 3D $O(N)$-models

by

Jonas Wattendorff, B.Sc.

Advisor: Priv.–Doz. Dr. Francesco Parisen-Toldin
Co-Advisor: Prof. Dr. Stefan Wessel

A thesis submitted in partial fulfillment
of the requirements for the degree of
Master of Science in Physics

Institute for Theoretical Solid State Physics
RWTH Aachen University
September 27, 2025

Contents

Chapter 1

Introduction

Critical phenomena and phase transitions are central topics in statistical mechanics. Among these phenomena, the critical Casimir force is particularly intriguing, as it arises when systems near a continuous phase transition are confined by boundaries. This thesis investigates the critical Casimir force in three-dimensional $O(N)$ models using Monte Carlo simulations.

The critical Casimir force appears in confined systems close to criticality, where long-ranged fluctuations of the order parameter are truncated by boundaries, leading to an effective force between them. A prominent experimental example is found in colloidal suspensions, where the attraction or repulsion of colloids near surfaces can be tuned by small temperature changes close to the solvent's critical point [1]. This tunability makes the critical Casimir effect promising for controlling colloidal suspensions in micro- and nano-mechanical applications [2].

Close to a continuous phase transition, physical systems display universal behavior characterized by critical exponents independent of microscopic details. This phenomenon is known as universality and is a key concept in the study of phase transitions. Renormalization-group theory explains the emergence of universality by the flow of Hamiltonians to fixed points in the space of couplings. Systems flowing to the same fixed points share identical universal properties. [3]

Renormalization-group arguments further show that confinement modifies universality. While the bulk critical behavior remains that of the unconfined system, the surface can belong to distinct universality classes depending on its symmetries and boundary conditions [3]. Thus, the study of surface critical behavior naturally complements the well-established understanding of bulk universality.

Classical $O(N)$ models provide the standard theoretical framework for analyzing critical Casimir forces. These models describe systems with N-component order parameters, encompassing the Ising ($N = 1$), XY ($N = 2$), and Heisenberg ($N = 3$) universality classes. Bulk properties of $O(N)$-models are known with high precision, which makes their surface and confinement-induced behavior the next logical step of investigation. Experimental observations in liquid ^{4}He, whose critical behavior belongs to the $O(2)$ universality class [4], further highlight the relevance of studying Casimir forces in $O(N)$ models.

The critical Casimir force is highly sensitive to boundary conditions. In the Ising universality class, this dependence has been explored extensively [5, 6, 7, 8]. However, for $O(N \geq 2)$-models, there are fewer results available, and for $N = 3$, even fewer. For $N = 2$, there are interesting mean-field results [9], which we aim to extend with Monte Carlo simulations in this thesis.

Monte Carlo methods are particularly well suited for investigating critical phenomena. They provide access to high-dimensional parameter spaces and enable the study of complex systems where analytic approaches are intractable. Moreover, established algorithms for the $O(N)$ model are known, yielding precise estimates of critical parameters and universal quantities [10, 11, 12, 13]. The flexibility of Monte Carlo algorithms allows straightforward extensions to different values of N and various boundary conditions, making them an ideal tool for studying the critical Casimir effect.

The remainder of this thesis is organized as follows. Chap. 2 introduces the theoretical framework underlying the critical Casimir force and its numer-

ical treatment. Chap. 3 describes the model and Monte Carlo methods employed. Chap. 4 presents our results for the critical Casimir force in $O(N)$ models with different boundary conditions, including comparisons with mean-field predictions and explorations of new geometries. Finally, Chap. 5 summarizes the main findings and outlines potential directions for future research.

Chapter 2

Boundary Critical Phenomena

There is a range of interesting phenomena that emerge when boundaries are applied to critical systems. For instance, understanding the effect of confinement enables the computational investigation of critical systems through finite-size scaling and real space renormalization group methods. Moreover, varying boundary conditions or tuning surface interactions in otherwise well-understood bulk models reveals additional rich physics [14, I. Introduction].

## 2.1 Critical Casimir Effect

The Casimir effect is most familiar from quantum electrodynamics, where two conducting plates experience an attractive force due to the confinement of massless, long-ranged fluctuations of the electromagnetic field [15]. Naturally, the question arises whether an analogous force exists in other systems with massless, long-ranged excitations confined by boundaries. In 1978 Fisher and Gennes found a similar effect in liquid binary mixtures, where critical fluctuations act as effective massless modes. Confining the system between two plates, whose distance is smaller than the correlation length ξ, leads to a net force [16]. Although the original work did not explicitly reference the Casimir effect, the term *critical Casimir effect* effect was later adopted to describe forces emerging from long-ranged fluctuations near continuous phase transitions.

In this thesis, we investigate the critical Casimir effect under various boundary conditions. Specifically, we restrict ourselves to parallel surfaces, with free boundary conditions in the direction orthogonal to the surfaces. On these surfaces, we can modify couplings to enhance or reduce interactions and apply external symmetry-breaking fields.

The bulk of a d-dimensional system contains N^d atoms, while the surfaces only hold N^{d-1} atoms, a fraction of $N^{-1/d}$, usually it is safe to neglect the surface effects on the bulk properties. However, near a critical point the correlation length ξ diverges, making the influence of the surface to the bulk properties more important. Still, in this thesis we assume, that the influence of the surface on bulk properties is small enough to split the free energy into bulk and surface contributions, proportional to L^d and L^{d-1}, respectively, where L is a characteristic system length. The bulk free energy exhibits universal scaling behavior independent of boundary conditions, while the surface free energy defines a distinct surface universality class determined by both the bulk universality class and boundary conditions. In this thesis, we observe the effect of different surface universality classes on the critical Casimir force.

Bringing the bulk near criticality $\beta_{c,\mathrm{bulk}}$ and tuning the surface coupling β_{surface} results in a rich phase diagram, as shown in Fig. 2.1. At $\beta_{\mathrm{bulk}} = \beta_{c,\mathrm{bulk}}$ the bulk is critical and orders for $\beta_{\mathrm{bulk}} > \beta_{c,\mathrm{bulk}}$. For $N = 1, 2$, however, the surface may exhibit (quasi) long-range order even if the bulk is disordered, as shown in Fig. 2.1 (a). The four phase transitions are

- the *ordinary transition* from (bulk, surface) = (disord., disord.) to (ord., ord.),

- the *extraordinary transition* from (disord., ord.) to (ord., ord.),

- the *surface transition* from (disord., disord.) to (disord., ord.),

- and the *special point*, where the three transi-
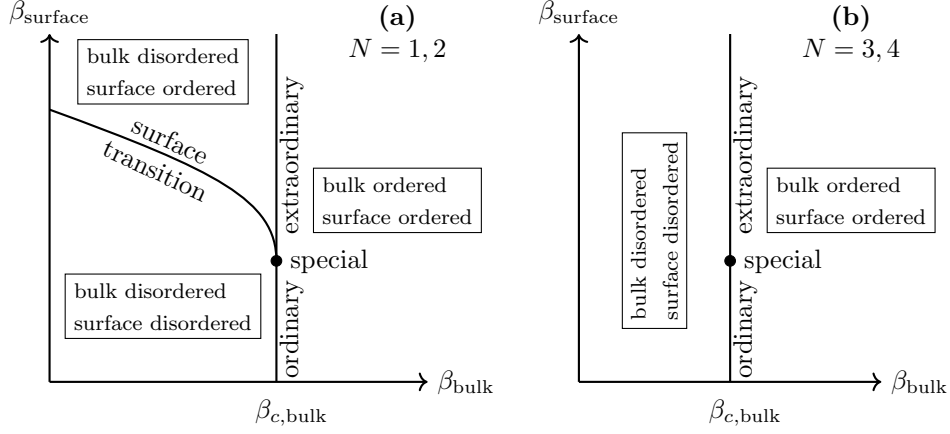
Fig. 2.1: A sketch of the phase diagram in the $\beta_{\text{bulk}}-\beta_{\text{surface}}$ plane of a system with surface enhancements. The parameter β is the coupling constant divided by the temperature. **(a)** for $N = 1, 2$ four transitions appear, ordinary, special, extraordinary, and the surface transition. **(b)** for $N = 3, 4$ the surface can no longer order by itself, so the surface transition disappears.

tions meet.

For $N = 3, 4$ the surface cannot order independently, so the surface transition is absent, as shown in Fig. 2.1 (b). The division of the vertical line at $\beta_{c,\text{bulk}}$ into ordinary, special, and extraordinary is no longer dictated by the topology of the phase diagram. Still, Monte Carlo simulations show that three distinct phase transitions remain. [17]

Yet another universality class arises when external surface fields are applied. While the bulk is not ordered by this perturbation, the surface flows to the *normal universality class* fixed point, where the surface orders in the direction of the surface field, independent of its strength.

In this thesis we focus on systems confined by two parallel surfaces, each of which can independently realize a different surface universality class. The resulting Casimir force exhibits a diverse behavior depending on the surface universality classes, so the behavior of the Casimir force is as rich as the phase diagram in Fig. 2.1. Moreover, if both surfaces are in the normal universality class, we observe that the Casimir force changes with the relative angle between the external fields, as we will discuss in detail.
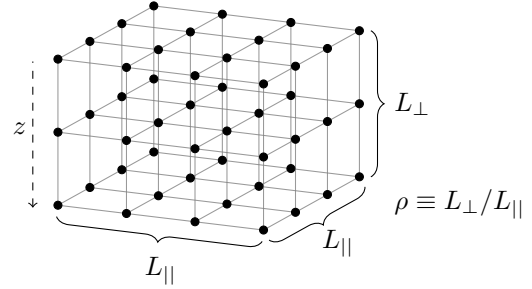
Fig. 2.2: Schematic of the lattice. Points denote lattice sites, lines indicate nearest-neighbor bonds.

2.2 Finite-Size Scaling

In this section, we will introduce the relevant finite-size scaling relations, used to derive the expression for the critical Casimir force in Eq. (2.9).

The system considered in this thesis is a three-dimensional cubic lattice with a continuous bulk phase transition at $T = T_c$. Along the x- and y-direction we impose periodic boundary conditions and set a side length of $L_x = L_y \equiv L_{||}$, such that $0 \leq x, y < L_{||}$. Along the z-direction we impose various boundary conditions and set a side length of $L_z \equiv L_\perp$ ($0 \leq z < L_\perp$). We define the aspect ratio of the slab as $\rho \equiv L_\perp/L_{||}$, e.g. a thin film corresponds to $\rho \ll 1$ and a cube to $\rho = 1$. A sketch of the lattice is shown in Fig. 2.2.

Sites are in the bulk if $0 < z < L_\perp - 1$ and on the

5

top (bottom) surface if $z = 0$ ($z = L_\perp - 1$). The bulk is free of external fields, only the surfaces may have symmetry-breaking external fields. Accordingly, in the RG scaling of the free energy the temperature is the only relevant bulk scaling variable.

For every thermodynamic system, in the vicinity of the critical point, $t = (T - T_c)/T_c = 0$, the free-energy density $\mathcal{F} = F/V$ in units of $k_B T$ decomposes into singular and non-singular contributions

$$\mathcal{F} = \mathcal{F}^{(s)} + \mathcal{F}^{(ns)}. \tag{2.1}$$

The non-singular term $\mathcal{F}^{(ns)}$ is analytic in t and dependent on the geometry of the system, with specific contributions from the bulk and surfaces

$$\mathcal{F}^{(ns)}(t, L_\perp, L_{||}) = f_{\text{bulk}}^{(ns)}(t) + \frac{1}{L_\perp} f_{\text{surface}}^{(ns)}(t) + O(e^{-\xi/L_\perp}/L_\perp), \tag{2.2}$$

other corrections are exponentially suppressed.

By contrast, the singular part $\mathcal{F}^{(s)}(t, L_\perp, L_{||})$ is non-analytic in at least one of its arguments. The scaling postulate dictates the finite-size dependence of the singular free energy [18, section 1.3]

$$\mathcal{F}^{(s)}(t, L_\perp, L_{||}) = \frac{1}{L_\perp^3} f(x_t, \rho),$$
$$x_t = t\left(L_\perp/\xi_0^+\right)^{1/\nu}, \tag{2.3}$$

where x_t is the temperature scaling variable, ν is the universal correlation-length exponent and ξ_0^+ is the non-universal amplitude of the bulk correlation length $\xi = \xi_0^+ |t|^{-\nu}$, for $t > 0$. The universal scaling function $f(x_t, \rho)$ only depends on the bulk universality class, the aspect ratio ρ, and the boundary conditions of the surfaces.

The bulk free energy density $f_{\text{bulk}}(t)$ is defined as the limit of an infinite system size

$$f_{\text{bulk}}(t) = \mathcal{F}(t, L_\perp \to \infty, L_{||} \to \infty). \tag{2.4}$$

It is independent of the boundary conditions, as surfaces do not interact in this limit. Analogous to Eq. (2.1), it splits into a singular and non-singular part

$$f_{\text{bulk}}(t) = f_{\text{bulk}}^{(s)}(t) + f_{\text{bulk}}^{(ns)}(t). \tag{2.5}$$

We define the excess free energy density f_{ex} as the difference of the free energy density $\mathcal{F}$ and the bulk contribution f_{bulk}

$$f_{\text{ex}}^{(s)}(t, L_\perp, L_{||}) = \mathcal{F}^{(s)}(t, L_\perp, L_{||}) - f_{\text{bulk}}^{(s)}(t). \tag{2.6}$$

The critical Casimir force per surface area $L_{||}^2$ and per $k_B T$ is defined as

$$F_C = -\frac{\partial\left(L_\perp f_{\text{ex}}^{(s)}\right)}{\partial L_\perp}. \tag{2.7}$$

From the scaling behavior of the free energy density in Eq. (2.3) we infer

$$F_C = \frac{1}{L_\perp^3} \theta\left(x_t, \rho\right), \tag{2.8}$$

where $\theta(x_t, \rho)$ is the *Casimir scaling function*, it determines whether the surfaces attract or repel. The value of the scaling function at criticality $\theta(0, \rho)$ is the *Casimir amplitude*.

This result holds up to system specific corrections to scaling contributions to θ arising from irrelevant scaling variables. Some scaling corrections are strongly suppressed by a intentional choice of model parameters, as explained in Sec. 3.1. Nevertheless, for the $O(N)$-model a residual correction proportional to $L_\perp^{-1}$ remains due to the ambiguity in defining the effective slab thickness. As argued in [19], the precise position of the surfaces is arbitrary on the scale of the lattice spacing. Furthermore, $L_\perp$ does no longer transform under RG as $L_\perp \to L_\perp/b$, so a new scaling field needs to be introduced, with the leading correction $L_\perp \to L_\perp + c'$. Note, the aspect ratio is also affected by this correction, $\rho \to (L_\perp + c')/L_{||}$. As shown in [20], θ is expanded in the second argument around $\rho = L_\perp/L_{||}$ up to order $1/L_\perp$. This correction is absorbed into a single parameter c, yielding the corrected scaling form of the Casimir force

$$F_C = \frac{1}{(L_\perp + c)^3} \theta(\bar{x}_t, \rho),$$
$$\bar{x}_t = t\left(\frac{L_\perp + c}{\xi_0^+}\right)^{1/\nu}, \tag{2.9}$$

where c is a function of the boundary conditions and aspect ratio ρ. These are the parameters and corrections used in the subsequent data analysis. [5]

Chapter 3

Model and Method

In Sec. 3.1 we introduce the lattice model used in the simulations. In Sec. 3.2 we present two methods for measuring the critical Casimir force in Monte Carlo simulations: the coupling parameter method in Sec. 3.2.1 and the temperature integration method in Sec. 3.2.2. In Sec. 3.3 we detail the Monte Carlo employed.

3.1 Lattice Model

All simulations were performed for a classical lattice ϕ^4-model, which is in the same universality class of the classical $O(N)$-model. The reduced hamiltonian is

$$\mathcal{H} = -\sum_{\langle i,j\rangle} \beta_{ij}\boldsymbol{\phi}_i \cdot \boldsymbol{\phi}_j + \sum_i \left[\boldsymbol{\phi}_i^2 + \lambda(\boldsymbol{\phi}_i^2 - 1)^2\right]$$
$$ - \sum_{i\in\text{surface}} \boldsymbol{h}_i \cdot \boldsymbol{\phi}_i, \quad (3.1)$$

where $\boldsymbol{\phi}_i$ are real N component spins and $\boldsymbol{h}_i$ are the external fields applied to the surfaces. The reduced couplings β_{ij} are the inverse temperature $1/k_BT$ multiplied by the coupling strength of the spins, such that the Gibbs measure is $\sim e^{-\mathcal{H}}$. In contrast to the $O(N)$-model, there is no hard-spin constraint, instead $\lambda > 0$ controls the amplitude fluctuations of the spins. The $O(N)$-model is recovered for $\lambda \to \infty$. For finite λ, the universal behavior remains in the $O(N)$-model universality class. We are using the ϕ^4-model instead of the $O(N)$-model because corrections to scaling are strongly suppressed for certain values of λ [21, 13, 10]. The parameter values used in the simulations are given in Sec. 3.3.5.

We work with a three-dimensional cubic lattice with periodic boundaries in x- and y-direction, and optionally periodic or free boundaries in the z-direction. The lattice extends $L_x = L_y \equiv L_{||}$ parallel to the surface and $L_z \equiv L_\perp$ orthogonal to the surface, with a lattice spacing set to 1. The external fields only act on the surfaces, while the bulk symmetry is never broken, as indicated in Eq. (3.1). We restrict ourselves to uniform fields on each surface, so $\boldsymbol{h}_i = \boldsymbol{h}_{\text{bottom}}$ on the bottom surface and $\boldsymbol{h}_i = \boldsymbol{h}_{\text{top}}$ on the top surface.

The parameters β_{ij} and λ control the bulk behavior of the system. The coupling β_{ij} can be different on the surface β_s than in the bulk β. In general

$$\beta_{ij} = \begin{cases} \beta, & \langle ij\rangle \in \text{bulk}, \\ \beta_s, & \langle ij\rangle \in \text{surface}. \end{cases} \quad (3.2)$$

The critical point of the bulk is located at (β_c, λ_c) in parameter space, the parameters (β_c, λ_c) depend on N.

Note that β is not the inverse temperature $1/k_BT$. In practice, we explore the phase transition by varying β at fixed $\lambda = \lambda_c$. Although this path through the β-λ phase-plane is different from changing the actual temperature, the universal properties remain the same and universal quantities can still be extracted.

3.2 Measuring Casimir Forces

In this section, we discuss two methods to measure the Casimir force in the lattice ϕ^4-model. In Sec. 3.2.1 we present the *coupling parameter method*, which efficiently extracts the Casimir force for a fixed temperature. In Sec. 3.2.2 we introduce the *temperature integration method*, which extracts the Casimir force over an extended temperature range.

3.2.1 Coupling Parameter

As derived in Sec. 2.2, the Casimir force is obtained from the free energy density. Monte Carlo methods are generally not efficient in computing quantities that cannot be expressed in ensemble averages, so the free energy F is not directly accessible. However, the free energy difference ΔF can be expressed in terms of ensemble averages with the coupling parameter method [22], and ΔF is sufficient to extract the Casimir scaling function.

The coupling parameter method gives the free energy difference between two systems $\Delta F = F_1 - F_0$. The two systems must be at the same temperature β and have the same configuration space $\mathcal{C}$, while the hamiltonians $\mathcal{H}_0$ and $\mathcal{H}_1$ may differ in couplings and symmetries. For lattice models this requires the same number of spins and the dimensionality of the spins, but the couplings may be different. The coupling parameter k couples the hamiltonians via a linear interpolation

$$\mathcal{H}_{\text{cr}}(k) = (1 - k)\mathcal{H}_0 + k\mathcal{H}_1, \ k \in [0, 1], \quad (3.3)$$

resulting in the crossover hamiltonian $\mathcal{H}_{\text{cr}}(k)$. The crossover hamiltonian interpolates between the two systems $\mathcal{H}_0$ and $\mathcal{H}_1$ while staying in the same configuration space $\mathcal{C}$. The crossover free energy $F_{\text{cr}}(k)$, in units of $k_B T$, interpolates between the two free energies F_0 and F_1

$$F_{\text{cr}}(k) = -\ln\left(\sum_{\mathcal{C}} e^{-\mathcal{H}_{\text{cr}}(k)}\right). \quad (3.4)$$

Then $dF_{\text{cr}}(k)/dk$ can be written both as an integral

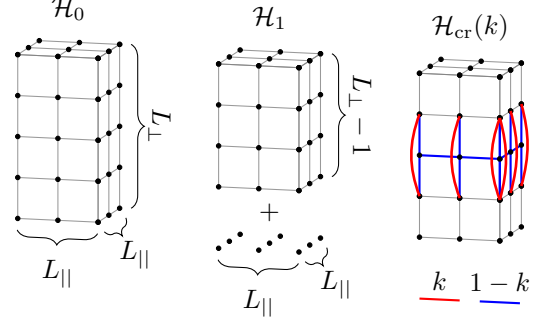$$F_1 - F_0 = \int_0^1 dk \frac{dF_{\text{cr}}(k)}{dk}. \quad (3.5)$$

and by explicitly differentiating Eq. (3.4)

$$\frac{dF_{\text{cr}}(k)}{dk} = \frac{\sum_{\mathcal{C}}(\mathcal{H}_1 - \mathcal{H}_0)e^{-\mathcal{H}_{\text{cr}}(k)}}{\sum_{\mathcal{C}} e^{-\mathcal{H}_{\text{cr}}(k)}} = \langle\Delta\mathcal{H}\rangle_k, \quad (3.6)$$

with $\Delta\mathcal{H} \equiv \mathcal{H}_1 - \mathcal{H}_0$. Combining Eqs. (3.5) and (3.6) gives

$$F_1 - F_0 = \int_0^1 dk \langle\Delta\mathcal{H}\rangle_k. \quad (3.7)$$

The integral is performed by estimating $\langle\Delta\mathcal{H}\rangle_k$ with standard Monte Carlo methods at several values of k (see Fig. 3.2) and integrating numerically.

Fig. 3.1: Sketch of the lattices used in the coupling parameter method. **Left**: $\mathcal{H}_0$. **Middle**: $\mathcal{H}_1$, where one layer is removed. **Right**: $\mathcal{H}_{\text{cr}}(k)$, where the middle layer has nearest neighbor interactions weighted with $1 - k$ and across-gap interactions weighted with k.

We choose $\mathcal{H}_0$ and $\mathcal{H}_1$ as shown in Fig. 3.1. The hamiltonian $\mathcal{H}_0$ is Eq. (3.1) for a slab of size $L_\perp \times L_{||} \times L_{||}$. In $\mathcal{H}_1$, one layer is removed, such a slab of size $(L_\perp - 1) \times L_{||} \times L_{||}$ with couplings as Eq. (3.1) and one non-interacting layer of size $1 \times L_{||} \times L_{||}$ remain. The hamiltonian of the free layer is

$$\mathcal{H}_{\text{free}} = \sum_i \left[\phi_i^2 + \lambda(\phi_i^2 - 1)^2\right]. \quad (3.8)$$

Effectively, one layer in the middle is continuously decoupled as $k = 0 \rightarrow k = 1$. In $\mathcal{H}_{\text{cr}}(k)$, one layer in the middle has nearest neighbor interactions $-(1 - k)\beta\phi_i \cdot \phi_j$, which are the red bonds in Fig. 3.1. The blue bonds in Fig. 3.1 are across-gap interactions with coupling $-k\beta\phi_i \cdot \phi_j$, restoring the connectivity. [7]

We define the free energy difference per surface area and per $k_B T$ as

$$I(\beta, L_\perp, L_{||}) = \frac{F_1 - F_0}{L_{||}^2} = \frac{1}{L_{||}^2} \int_0^1 dk \langle\Delta\mathcal{H}\rangle_k. \quad (3.9)$$

Fig. 3.2 shows $\langle\Delta\mathcal{H}\rangle_k/L_{||}^2$ as a function of the coupling parameter k. The exact k position of the data points is given by the Gauß-Kronrod integration rule, described below.

Using Eqs. (2.2) and (2.6) the free energies F_0 and F_1 are decomposed into bulk, surface and excess contributions

$$F_0 = L_\perp L_{||}^2[f_{\text{bulk}}(t) + f_{\text{ex}}^{(s)}(t, L_\perp, L_{||})] + L_{||}^2 f_{\text{surface}}^{(ns)}(t), \quad (3.10)$$
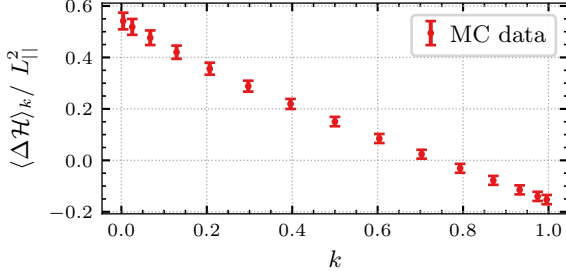
Fig. 3.2: Plot of $\langle \Delta \mathcal{H} \rangle_k / L_{||}^2$ as a function of the coupling parameter k. The error bars are scaled up by 10^3.

and

$$F_1 = (L_\perp - 1)L_{||}^2[f_{\text{bulk}}(t) + f_{\text{ex}}^{(s)}(t, L_\perp - 1, L_{||})]$$
$$+ L_{||}^2 f_{\text{surface}}^{(ns)}(t) + L_{||}^2 f_{\text{free}}(t), \quad (3.11)$$

where $f_{\text{free}}(t)$ is the contribution of the free layer of spins in $\mathcal{H}_1$. Inserting these into $I(\beta, L_\perp, L_{||})$ we get

$$I(\beta, L_\perp, L_{||}) = [f_{\text{free}}(t) - f_{\text{bulk}}(t)] - \Delta f_{\text{ex}}^{(s)}(t, L_\perp, L_{||})$$
$$(3.12)$$

where

$$\Delta f_{\text{ex}}^{(s)}\left(t, L_\perp - 1/2, L_{||}\right) = L_\perp f_{\text{ex}}^{(s)}(t, L_\perp, L_{||})$$
$$- (L_\perp - 1)f_{\text{ex}}^{(s)}(t, L_\perp - 1, L_{||}). \quad (3.13)$$

Taylor expanding Eq. (3.13) around $L_\perp - \frac{1}{2}$ yields

$$\Delta f_{\text{ex}}^{(s)} = \left.\frac{\partial \left(L_\perp f_{\text{ex}}^{(s)}\right)}{\partial L_\perp}\right|_{L_\perp - \frac{1}{2}} + \ldots, \quad (3.14)$$

retaining the leading term while neglecting scaling corrections $O(L_\perp^{-2})$. From Eq. (2.7) we identify the Casimir force $\partial \left(L_\perp f_{\text{ex}}^{(s)}\right) / \partial L_\perp = -F_C$. Combining Eqs. (3.12) and (3.14) gives

$$I(\beta, L_\perp, L_{||}) = [f_{\text{free}}(t) - f_{\text{bulk}}(t)]$$
$$+ F_C\left(t, L_\perp - 1/2, L_{||}\right). \quad (3.15)$$

Note, the Casimir force of a system of size $(L_\perp - 1/2) \times L_{||} \times L_{||}$ is measured. Inserting the scaling form of the Casimir force from Eq. (2.9) with $L_\perp \to L_\perp - 1/2$ gives

$$I(\beta, L_\perp, L_{||}) = B(t) + \frac{\theta\left(\tilde{x}_t, \tilde{\rho}\right)}{(L_\perp - 1/2 + c)^3}, \quad (3.16)$$
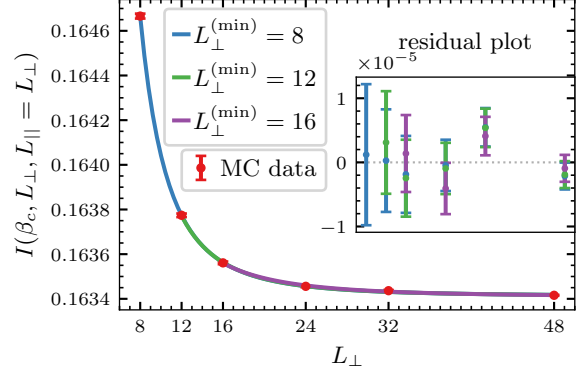
Fig. 3.3: Monte Carlo data fitted against Eq. (3.16) for three values of $L_\perp^{(\text{min})}$. The inset shows the residuals of the three fits, where the colors match the corresponding fits. The data is from a $N = 2$ ϕ^4-model with $\rho = 1$, $\beta = \beta_c$, and ordinary boundary conditions.

where the aspect ratio $\tilde{\rho}$ and scaling field $\tilde{x}_t$ have the appropriate corrections

$$\tilde{\rho} = \frac{L_\perp - 1/2}{L_{||}}, \quad \tilde{x}_t = t \left(\frac{L_\perp - 1/2 + c}{\xi_0^+}\right)^{1/\nu}. \quad (3.17)$$

We fit B, c, and θ against Monte Carlo data as a function of $L_\perp$. Fig. 3.3 demonstrates how the fit is performed. The x-axis is the distance between the surfaces $L_\perp$, the y-axis is the free energy difference $I(\beta_c, L_\perp, L_{||} = L_\perp)$ from Eq. (3.9) at the critical point. The parameter $L_\perp^{(\text{min})}$ stands for the smallest $L_\perp$ included in the fit. The stability of the fit parameters is assessed by varying $L_\perp^{(\text{min})}$, the numeric values are shown in Tab. 3.1. Fits $L_\perp^{(\text{min})} = 8$ and $L_\perp^{(\text{min})} = 12$ are consistent with each other, while $L_\perp^{(\text{min})} = 16$ has relatively large errors in θ and c and an unfavorable goodness of fit χ^2/dof, presumably due to too having few data points with large relative uncertainties. The inset of Fig. 3.3 shows that the residuals of the fits remain consistent for all $L_\perp^{(\text{min})}$. In this case we trust the fit result for $L_\perp^{(\text{min})} = 8$. This is the general procedure to extract the Casimir amplitude θ with the coupling parameter method. $L_\perp^{(\text{min})}$ is reassessed for each system separately. [20]

The integral in Eq. (3.9) is evaluated numerically using the Gauß–Kronrod rule. Compared with, for example, the trapezoidal rule, fixed-node quadrature rules achieve higher accuracy for a given number of nodes. The nodes $\{k_{\text{GK}}\}$ and weights

$L_{\min}$	B	θ	c	χ^2/dof
8	$0.163\,412\,5\,(18)$	$0.592\,(32)$	$0.29\,(15)$	$1.5\,(0.8)$
12	$0.163\,412\,1\,(22)$	$0.62\,(9)$	$0.5\,(6)$	$2.2\,(1.0)$
16	$0.163\,409\,5\,(32)$	$0.92\,(31)$	$2.8\,(2.1)$	$3.0\,(1.4)$

Tab. 3.1: Fit parameters from Fig. 3.3.
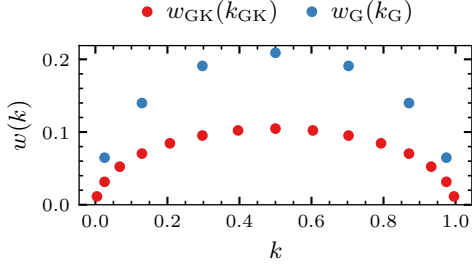
Fig. 3.4: Plot of Gauß-Kronrod nodes and weights for the 15/7 quadrature rule.

$w_{\mathrm{GK}}(k_{\mathrm{GK}})$, tabulated in [23], are used to approximate the integral

$$I(\beta, L_\perp, L_{||}) \approx I_{\mathrm{GK}}(\beta, L_\perp, L_{||})$$
$$= \frac{1}{L_{||}^2} \sum_{\{k_{\mathrm{GK}}\}} w_{\mathrm{GK}}(k_{\mathrm{GK}}) \langle \Delta \mathcal{H} \rangle_{k_{\mathrm{GK}}}. \tag{3.18}$$

A key property is the existence of a subset $\{k_{\mathrm{G}}\} \subset \{k_{\mathrm{GK}}\}$, that itself forms a valid quadrature rule with weights $w_{\mathrm{G}}(k_{\mathrm{G}})$. We are using the 15/7 Gauß-Kronrod rule, meaning 15 Gauß–Kronrod nodes and 7 Gauß nodes, the nodes and weights are plotted in Fig. 3.4. The difference between the 15 node rule I_{GK} and the 7 node rule I_{G} provides an estimate of the systematic quadrature error. In our simulations this systematic error is negligible compared to the statistical error. [23]

3.2.2 Temperature Integration

For the coupling parameter method the temperature scaling variable x_t has to be fixed, which is trivial at criticality since $x_t = 0$. However, for $\beta \neq \beta_c$ keeping constant would require rescaling $L_\perp$ with β, which is inconvenient and computationally expensive. Instead, we use the temperature integration method [24], keeping $L_\perp$ fixed over the full temperature range. Starting from the reduced free energy density

$$\mathcal{F} = -\frac{1}{L_\perp L_{||}^2} \log Z, \tag{3.19}$$

where Z is the canonical partition function, we define the internal energy density per $k_B T$ as

$$E = -\frac{1}{L_\perp L_{||}^2} \frac{\partial \log Z}{\partial \beta}. \tag{3.20}$$

As mentioned in the beginning of Sec. 3.1, β is not strictly speaking the inverse temperature, but this definition is convenient for computations and gives the universal quantities. Differentiating Eq. (3.1) yields

$$E = -\frac{1}{L_\perp L_{||}^2} \left\langle \sum_{\langle ij \rangle} \phi_i \cdot \phi_j \right\rangle, \tag{3.21}$$

for the Casimir scaling function we only consider the case $\beta_s = \beta$, further research could explore the dependence on β_s. The expectation value in Eq. (3.21) is calculated with standard Monte Carlo methods. The left panel of Fig. 3.5 shows the internal energy density for the bulk and two slabs of different thickness.

Combining Eqs. (3.19), (3.20) and (3.21) gives

$$\mathcal{F}(\beta) = \mathcal{F}(\beta_0) - \int_{\beta_0}^{\beta} d\beta' E(\beta'). \tag{3.22}$$

Using Eq. (2.6), the excess free energy density is

$$f_{\mathrm{ex}}^{(s)}(\beta) = \mathcal{F}(\beta_0) - f_{\mathrm{bulk}}(\beta) - \int_{\beta_0}^{\beta} d\beta' E(\beta'). \tag{3.23}$$

Similarly the bulk free energy density $f_{\mathrm{bulk}}(\beta)$ is

$$f_{\mathrm{bulk}}(\beta) = f_{\mathrm{bulk}}(\beta_0) - \int_{\beta_0}^{\beta} d\beta' E_{\mathrm{bulk}}(\beta'), \tag{3.24}$$

where $E_{\mathrm{bulk}}(\beta')$ is computed with Eq. (3.21) on large, fully periodic lattices. The boundary values $f_{\mathrm{bulk}}(\beta_0)$ and $\mathcal{F}(\beta_0)$ are calculated with the coupling parameter method, as described below. As in
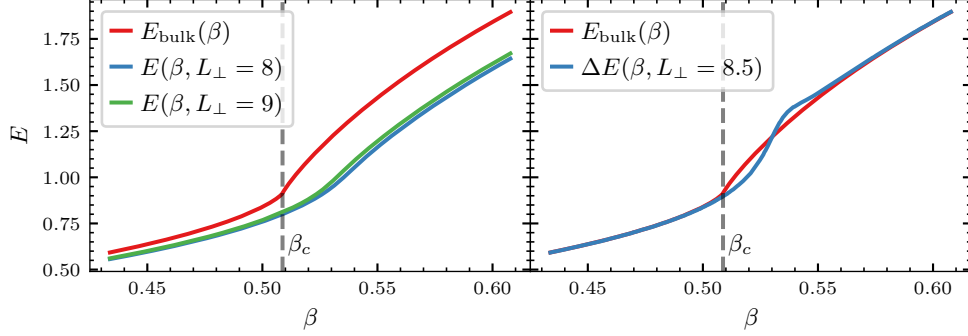
Fig. 3.5: Left: internal energy densities of bulk (Tab. 3.2) and slabs of sizes $8 \times 32 \times 32$ and $9 \times 32 \times 32$ (Tab. 3.3), in the $N = 2$ ϕ^4-model. **Right:** bulk energy density and slab internal energy difference.

Eq. (3.14), we approximate the Casimir force with

$$F_C = -\frac{\partial \left(L_\perp f_{\text{ex}}^{(s)} \right)}{\partial L_\perp} \approx -\Delta f_{\text{ex}}^{(s)}. \qquad (3.25)$$

Combining Eqs. (3.13), (3.23), (3.24), and (3.25) yields, for a system of size $(L_\perp - 1/2) \times L_{||} \times L_{||}$,

$$F_C(\beta) = F_C(\beta_0) + \int_{\beta_0}^{\beta} d\beta' [\Delta E(\beta') - E_{\text{bulk}}(\beta')], \qquad (3.26)$$

with

$$\Delta E(\beta, L_\perp - 1/2, L_{||}) = L_\perp E(\beta, L_\perp, L_{||}) \\ - (L_\perp - 1) E(\beta, L_\perp - 1, L_{||}). \quad (3.27)$$

The quantities E_{bulk} and ΔE are shown in the right panel of Fig. 3.5, they separate near the critical point β_c, as expected from the critical Casimir effect, and coincide for high and low temperatures.

The boundary value $F_C(\beta_0, L_\perp - 1/2, L_{||})$ is calculated from the coupling parameter method. Although it goes to zero for $\beta_0 \to 0$, it is a non-negligible correction for typical integration ranges used in the simulations. From Eq. (3.15) we have

$$F_C \left(\beta_0, L_\perp - 1/2, L_{||} \right) = I(\beta_0, L_\perp, L_{||}) \\ - [f_{\text{free}}(\beta_0) - f_{\text{bulk}}(\beta_0)]. \quad (3.28)$$

Additionally, we simulate a large periodic system ($L_\perp = L_{||} = 128$) with the coupling parameter method, for which we are sure that the Casimir force F_C vanishes within uncertainties, giving

$$I_{\text{bulk}}(\beta_0) = [f_{\text{free}}(\beta_0) - f_{\text{bulk}}(\beta_0)]. \qquad (3.29)$$

The difference of Eqs. (3.28) and (3.29) yields the boundary value

$$F_C \left(\beta_0, L_\perp - 1/2, L_{||} \right) = I(\beta_0, L_\perp, L_{||}) - I_{\text{bulk}}(\beta_0). \qquad (3.30)$$

Finally with Eq. (2.9) we arrive at the Casimir scaling function for a system of size $(L_\perp - 1/2) \times L_{||} \times L_{||}$

$$\theta(\beta) = (L_\perp - 1/2 + c)^3 \left\{ I(\beta_0) - I_{\text{bulk}}(\beta_0) \right. \\ \left. - \int_{\beta_0}^{\beta} d\beta' [\Delta E(\beta') - E_{\text{bulk}}(\beta')] \right\}. \quad (3.31)$$

The correction to scaling $L_\perp \to L_\perp + c$ is the same as for the coupling parameter method in Eq. (3.16), the notation $\tilde{L}_\perp$ is defined in Eq. (3.17). [20]

The integral in Eq. (3.31) is evaluated using Simpson's rule [25, Chap. 4] with error propagation. To estimate the systematic error we integrate once using all data points and once using only every second data point. Fig. 3.6 shows the difference, with all statistical errors propagated through. The deviation is at most about one error bar from zero, which means that the systematic error is negligible compared with statistical errors. If the systematic error was larger, we would have to increase the density in β.

Tab. 3.2 summarizes the lattice sizes and β-ranges used for $E_{\text{bulk}}(\beta)$. Near the critical point the correlation length ξ drastically increases, requiring larger lattice sizes to only capture the bulk behavior. A few points near criticality are fitted additionally because $L = 256$ is not quite large enough. Tab. 3.3

11
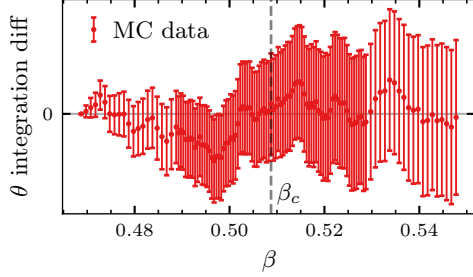
Fig. 3.6: Difference between the Simpson integration using all data points and using every second data point. Same dataset as in Fig. 3.5.

N	$L_\perp$	ranges and step size
2	9	$[-0.1, -0.02] \cup [0.02, 0.1]$ in 0.0005, $[-0.019\,75, 0.019\,75]$ in $0.000\,25$
	17	$[-0.04, -0.02] \cup [0.02, 0.04]$ in 0.0005, $[-0.019\,75, 0.019\,75]$ in $0.000\,25$
	33	$[-0.015, 0.015]$ in $0.000\,25$
3	9	$[-0.1, 0.1]$ in 0.0005
	17	$[-0.04, 0.04]$ in 0.0005

Tab. 3.3: Ranges and step sizes for the numerical integration in Eq. (3.31) for $N = 2, 3$ and various lattice thicknesses $L_\perp$. The ranges are given relative to $\beta_c^{(N=2)} = 0.508\,749\,88$ and $\beta_c^{(N=3)} = 0.687\,985\,21$.

N	L	$\beta_{\min}$	$\beta_{\max}$	$\Delta\beta$
2	32	$0.408\,749\,88$	$0.608\,249\,88$	0.0005
	48	$0.458\,749\,88$	$0.558\,249\,88$	0.0005
	64	$0.488\,749\,88$	$0.528\,499\,88$	$0.000\,25$
	96	$0.488\,749\,88$	$0.528\,499\,88$	$0.000\,25$
	128	$0.498\,749\,88$	$0.518\,499\,88$	$0.000\,25$
	192	$0.498\,749\,88$	$0.518\,499\,88$	$0.000\,25$
	256	$0.498\,749\,88$	$0.518\,499\,88$	$0.000\,25$
3	32	$0.587\,985\,21$	$0.787\,485\,21$	0.0005
	64	$0.637\,985\,21$	$0.737\,485\,21$	0.0005
	96	$0.662\,985\,21$	$0.712\,485\,21$	0.0005
	128	$0.662\,985\,21$	$0.712\,485\,21$	0.0005
	256	$0.662\,985\,21$	$0.712\,485\,21$	0.0005

Tab. 3.2: Ranges and step sizes used for determining $E_{\text{bulk}}(\beta)$ for $N = 2, 3$. Various lattice sizes L are used. The range starts at $\beta_{\min}$ and ends at $\beta_{\max}$ with a step size of $\Delta\beta$.

summarizes the ranges and step sizes used to integrate Eq. (3.31).

3.3 Monte Carlo Simulation

Monte Carlo simulations generate equilibrium ensembles by evolving a system in time through a sequence of random updates given by a pseudo-random number generator. The evolution is non-deterministic, unlike Newton's or Schrödinger's equations, so independent runs from identical initial conditions produce different measurement results. However, these results converge to the same statistical averages within statistical error. [26, Chap. 1]

These methods are particularly powerful in statistical physics, where equilibrated systems move through high-dimensional phase spaces. While the exact microscopic dynamics are not followed, re-peated sampling of the phase space converges to the correct measurement of observables. The error of these measurements decreases as the number of statistically independent samples increases.

In the following sections we introduce Markov Chain Monte Carlo framework and describe implementation of the Metropolis, Overrelaxation and Wolff cluster updates. We then discuss details of the Monte Carlo simulations, such as choice of parameters, number of measurements, and error estimation.

3.3.1 Markov Chains

Markov chains are the theoretical basis for Monte Carlo simulations, they describe the stochastic time evolution of a system through phase space. For a system updated stochastically at discrete times $t_1, t_2, \ldots$, let the system be in discrete states $S_1, S_2, \ldots$, and denote the system at time t as $X_t \in \{S_i\}$. Consider the conditional probability P of transitioning into state $X_{t_n} = S_{i_n}$ given a chain of preceding states $X_{t_{n-1}} = S_{i_{n-1}}, \ldots, X_{t_1} = S_{i_1}$

$$P(X_{t_n} = S_{i_n} | X_{t_{n-1}} = S_{i_{n-1}}, \ldots, X_{t_1} = S_{i_1}). \tag{3.32}$$

This time evolution of X_t is called Markov process, if the conditional only depends on the immediate predecessor

$$P(X_{t_n} = S_{i_n} | X_{t_{n-1}} = S_{i_{n-1}}). \tag{3.33}$$

We introduce the notation

$$W_{ij} = P(X_{t_n} = S_i | X_{t_{n-1}} = S_j), \tag{3.34}$$

which makes it clear, that $\boldsymbol{W}$ is a transition matrix acting on the state vector $\boldsymbol{S}$ and W_{ij} does not depend on time t_n. The probability to be in state S_i

at time t_n is

$$P(X_{t_n} = S_i) = W_{ij}P(X_{t_{n-1}} = S_j). \qquad (3.35)$$

Promoting the discrete times t_i to a continuous variable t, we define

$$P_i(t) = P(X_t = S_i), \qquad (3.36)$$

for the probability of being in state S_i at time t. The Markov master equation

$$\frac{\partial P_i(t)}{\partial t} = \sum_j \left[W_{ji}P_j(t) - W_{ij}P_i(t) \right], \qquad (3.37)$$

is a differential equation, that describes the time evolution of the probability distribution $P_i(t)$.

There are three conditions $\boldsymbol{W}$ has to obey, such that for $t \to \infty$ we arrive at the ground state distribution of the system P^{eq}.

1. Normalization:

$$\sum_j W_{ij} = 1, \quad W_{ij} \geq 0. \qquad (3.38)$$

2. Ergodicity: If $P^{\mathrm{eq}}(S_i) > 0$ and $P^{\mathrm{eq}}(S_j) > 0$, there exist an $n \in \mathbb{N}$ such that $(\boldsymbol{W}^n)_{ij} > 0$.

3. Stationarity:

$$\sum_j W_{ij}P_j^{\mathrm{eq}} = P_i^{\mathrm{eq}} \qquad (3.39)$$

The transition probabilities $\boldsymbol{W}$ are not unique and can be freely chosen. A straightforward way to fulfill homogeneity in Eq. (3.39) is the detailed balance condition

$$W_{ij}P_j^{\mathrm{eq}} = W_{ji}P_i^{\mathrm{eq}}. \qquad (3.40)$$

Inserting detailed balance into Eq. (3.37) gives $\partial P_n^{\mathrm{eq}}(t)/\partial t = 0$. [26, Chap. 2] [27]

3.3.2 Metropolis Update

A simple yet effective algorithm to construct a Markov chain is the Metropolis update [28]. One update entails selecting a random site, proposing a trial update of its spin and accepting or rejecting the proposal based on the energy difference between the initial and trial state.

The goal is to find a correct and efficient transition matrix $\boldsymbol{W}$. We want it to fulfill the three

conditions from Sec. 3.3.1 and detailed balance. The probability of S_n occurring in ground state is

$$P_i(t) = \frac{e^{-\beta E_i}}{Z}. \qquad (3.41)$$

The partition function Z is not exactly known for big and complex systems. To get around this, we rearrange the detailed balance condition in Eq. (3.40) to get

$$W_{ij} = W_{ji}\frac{P_j^{\mathrm{eq}}}{P_i^{\mathrm{eq}}} = W_{ji}e^{-\beta\Delta E}, \qquad (3.42)$$

where $\Delta E = E_j - E_i$. The transition probabilities W_{ij} and W_{ji} only depend on the energy difference ΔE between consecutive states. A simple choice is

$$W_{ji} = \begin{cases} e^{-\beta\Delta E}, & \Delta E > 0, \\ 1, & \Delta E \leq 0. \end{cases} \qquad (3.43)$$

In summary, we propose based on the initial state S_i some new state S_j, by applying a spin update. The energy difference between the states ΔE can be efficiently calculated in many models. If S_j is energetically favorable, we accept it. If S_j is energetically unfavorable, we only accept it with a probability $e^{-\beta\Delta E}$, otherwise S_i is kept. [26, Chap. 4]

For the ϕ^4-model, one sweep involves $NL_\perp L_\parallel^2$ Metropolis updates, every component of every spin is updated once. For each component the update

$$\phi_i'^{(\alpha)} = \phi_i^{(\alpha)} + r\Delta \qquad (3.44)$$

is proposed and accepted with the probability of Eq. (3.43). Here, r is a uniform random number in $[-0.5, 0.5]$ and Δ is a parameter that is chosen for each system separately, such that the acceptance rate is around $0.4 \ldots 0.6$. Computing the energy difference ΔE only requires the neighboring spins of ϕ_i and the external fields, which makes this update computationally efficient.

3.3.3 Overrelaxation Update

The Overrelaxation update is a microcanonical and deterministic movement in state space, the energy is invariant and each state has only one possible successor. The idea is to rotate a spin as far as possible without changing the energy of the system. [29] [26, Chap. 5]

Given a lattice site i, the vector $\boldsymbol{\phi}_{i,\mathrm{nn}}$ is the local field interacting with the spin $\boldsymbol{\phi}_i$

$$\boldsymbol{\phi}_{i,\mathrm{nn}} = \sum_{\langle ij \rangle} \beta_{ij} \boldsymbol{\phi}_j + \boldsymbol{h}_i. \qquad (3.45)$$

For $N > 1$ there is at least one direction the spin may rotate to, without changing the energy of the system. The furthest of these rotations is given by

$$\boldsymbol{\phi}_i' = 2 \frac{\boldsymbol{\phi}_i \cdot \boldsymbol{\phi}_{i,\mathrm{nn}}}{\boldsymbol{\phi}_{i,\mathrm{nn}}^2} \boldsymbol{\phi}_{i,\mathrm{nn}} - \boldsymbol{\phi}_i. \qquad (3.46)$$

In principle this update is always accepted, but for numerical stability, we reject updates, where $\boldsymbol{\phi}_{i,\mathrm{nn}}^2 < 10^{-12}$. While this update is not ergodic, doing it between Metropolis and Wolff sweeps improves the movement through state space, decreasing autocorrelation times, with small computational cost. [30]

3.3.4 Wolff Cluster Update

As a system approaches the critical point, the divergence of spatial and temporal correlations go hand in hand. The autocorrelation time τ scales with the correlation length ξ as

$$\tau \sim \xi^z, \qquad (3.47)$$

where z is the nonuniversal dynamic critical exponent. This *critical slowing down* hinders simulations near the critical point, which is the region of interest for the Casimir effect. Cluster algorithms weaken this issue by performing non-local updates that flip entire spin clusters while preserving detailed balance. Such updates measurably reduce autocorrelation times, effectively lower the dynamic exponent z, and are computationally efficient, with the Wolff cluster update being the default choice. [26, Chap. 5]

Fortuin and Kasteleyn

A key insight comes from Fortuin and Kasteleyn, who discovered a mapping of the q-state Potts model to the percolation model [31]. In the q-state Potts model, each spin σ_i takes on q spin values, which interact via $-2\beta_{ij}(\delta_{\sigma_i \sigma_j} - 1)$ for neighboring spins. The model maps to bond percolation with probabilities

$$p_{ij} = 1 - e^{-2\beta_{ij}\delta_{\sigma_i\sigma_j}}. \qquad (3.48)$$
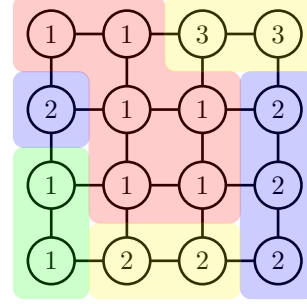
Fig. 3.7: Sketch of hypothetical lattice for $q = 3$, with clusters generated using Eq. (3.48). The integers in the circles represent the spin value q. Different colors represent different clusters.

Under this mapping, the partition functions of the models are the same $Z_{\mathrm{Potts}} = Z_{\mathrm{Percolation}}$ and thus all thermodynamic quantities are indistinguishable. The clusters in the bond percolation model are guaranteed to have uniform spin in the q-state Potts model according to Eq. (3.48). Furthermore, reassigning a cluster's spin value leaves the bond probabilities p_{ij}, hence the partition function $Z_{\mathrm{Potts}} = Z_{\mathrm{Percolation}}$, invariant. Thus all clusters can be independently assigned new spin values while obeying detailed balance.

Swendsen and Wang

Building on the Fortuin-Kasteleyn mapping, Swendsen and Wang formulated a Monte Carlo update [32]. Given some q-state Potts model configuration, construct an equivalent bond percolation lattice with the bond probabilities from Eq. (3.48), keep track of the clusters, then reassigning each cluster a random spin value. Fig. 3.7 shows a possible configuration of clusters is for $q = 3$. The update is ergodic, each site has a chance to be a single cluster which can be assigned any spin value, so every configuration is reachable. For systems close to criticality this update changes the position in state space rapidly, suppressing the critical slowing down significantly. [26, Chap. 5]

Wolff

Wolff extended the Swendsen-Wang update to $O(N)$-models and improved performance by updating only one cluster each step. Larger clusters occupy more space on the lattice, a randomly chosen site is more

likely to be part of a larger than average cluster. Flipping larger clusters moves the system quicker through state space, improving performance. [33]

The continuous ϕ^4 spins $\boldsymbol{\phi}_i$ are projected onto one randomly chosen direction $\boldsymbol{r}$: $\phi_i^{(\boldsymbol{r})} = \boldsymbol{\phi}_i \cdot \boldsymbol{r}$. The projected Ising (2-state Potts) interaction is

$$-\beta_{ij}\phi_i^{(\boldsymbol{r})}\phi_j^{(\boldsymbol{r})}. \tag{3.49}$$

Extracting discrete Ising spins $\sigma_i \in \{0,1\}$, with $\phi_i^{(\boldsymbol{r})} = |\phi_i^{(\boldsymbol{r})}|\sigma_i$, and treating the remaining terms as a coupling parameter gives

$$-\beta_{ij}^{(\boldsymbol{r})}(2\delta_{\sigma_i\sigma_j} - 1) = -\beta_{ij}\left|\phi_i^{(\boldsymbol{r})}\phi_j^{(\boldsymbol{r})}\right|(2\delta_{\sigma_i\sigma_j} - 1). \tag{3.50}$$

The mapping to the bond percolation model from Eq. (3.48) yields

$$p_{ij} = 1 - e^{-2\beta_{ij}^{(\boldsymbol{r})}\delta_{\sigma_i\sigma_j}}. \tag{3.51}$$

Starting from a random site i with spin ϕ_i, bonds are added to each neighbor ϕ_j with probability p_{ij}. Repeating this recursively for each added neighbor, a cluster of connected sites is grown. The original ϕ^4-spins are reflected with the matrix $\boldsymbol{R_r}$ along the plane perpendicular to $\boldsymbol{r}$

$$\boldsymbol{\phi}' = \boldsymbol{R_r}\boldsymbol{\phi}, \tag{3.52}$$

$$\boldsymbol{R_r} = \mathbb{1} - 2\boldsymbol{r}\boldsymbol{r}^T. \tag{3.53}$$

Flipping the cluster (*Wolff cluster*) preserves detailed balance in accordance to the Fortuin-Kasteleyn mapping. One flip constitutes one Wolff cluster update. [26, Chap. 5]

Ghost Spin Method

The Wolff cluster update is based on a $\mathbb{Z}_2$ symmetry of the projected Ising system. This symmetry is broken when an external field acts on the spins, as in Eq. (3.1), invalidating the detailed balance condition for cluster flips.

Accordingly, we introduce the *ghost spin* $\boldsymbol{\Phi}_g \in O(N)$, a new degree of freedom, initialized to $\boldsymbol{\Phi}_g = \mathbb{1}$ [34]. During construction of the Wolff cluster, it is treated as a neighbor to every site on the lattice. A bond between ghost site and normal sites is added with probability

$$p_{ij} = 1 - e^{-2\max\left(0, h_i^{(\boldsymbol{r})}\phi_i^{(\boldsymbol{r})}\right)}, \tag{3.54}$$

analogously to Eq. 3.51, where $h_i^{(\boldsymbol{r})} = \boldsymbol{h}_i \cdot \boldsymbol{r}$. The max() function ensures a non-negative bond probability. If the ghost spin is added to the cluster, all of its neighboring bonds are checked as usual. Trivially the ghost site only connects to sites experiencing a non-zero external field.

When flipping the cluster, all the spins are reflected as in Eq. (3.52). If the external field is part of the cluster, it is reflected similarly

$$\boldsymbol{h}' = \boldsymbol{R_r}\boldsymbol{h}. \tag{3.55}$$

The ghost spin $\boldsymbol{\Phi}_g$ is updated by right multiplying with $\boldsymbol{R_r^{-1}}$

$$\boldsymbol{\Phi}'_g = \boldsymbol{\Phi}_g\boldsymbol{R_r^{-1}}. \tag{3.56}$$

Effectively, $\boldsymbol{\Phi}_g$ keeps track of the direction changes of the external field. The magnetization (Eq. (3.61)) of the system with respect to the original external field is

$$\boldsymbol{m}' = \boldsymbol{\Phi}_g\boldsymbol{m}. \tag{3.57}$$

In this way the Wolff cluster update extends to systems with an external fields while preserving detailed balance.

3.3.5 Details of the Simulation

We run multiple copies of the same simulation with independent random numbers in parallel, directly average the measured observables, which is a first binning step. In practice we have $16 \dots 96$ cores, each running one simulation.

Initialization

The Monte Carlo simulation of the ϕ^4-model starts with the initialization of the lattice spins. We set the spin magnitudes to match the high temperature distribution. The spins decouple in this limit and the one spin partition function is

$$Z_1(N, \lambda) = S_{N-1}\int_0^\infty \phi^{N-1}e^{-\phi^2 - \lambda(\phi^2-1)^2}\,d\phi, \tag{3.58}$$

where S_{N-1} is the surface area of the $N-1$-dimensional unit sphere. The mean magnitude is

$$\bar{\phi} = \frac{S_{N-1}}{S_N}\frac{Z_1(N+1, \lambda)}{Z_1(N, \lambda)}, \tag{3.59}$$

and the standard deviation is

$$\sigma_\phi^2 = \frac{S_{N-1}}{S_{N+1}}\frac{Z_1(N+2, \lambda)}{Z_1(N, \lambda)} - \bar{\phi}^2. \tag{3.60}$$

	$\bar{\phi}$	σ_ϕ
$N = 1$	0.636	0.355
$N = 2$	0.869	0.260
$N = 3$	0.968	0.159
$N = 4$	0.997	0.082

Tab. 3.4: Spin magnitudes for the ϕ^4-model in the high temperature limit.

The partition functions are calculated numerically, the results are listed in Tab. 3.4.

Monte Carlo Step

The Monte Carlo steps are identical and performed until the accuracy requirements of the observables are met. One step consists of

1. a Metropolis sweep ($NL_\perp L_{||}^2$ updates),

2. an Overrelaxation sweep ($L_\perp L_{||}^2$ updates),

3. and a Wolff cluster update (variable number of updates).

Typically we perform $L_\perp$ Wolff updates, at criticality we expect the Wolff cluster size to be $\sim L^2$ for some system length scale L, so that in total $\sim L^3$ sites are flipped per step. At low temperatures the clusters become quite large, significantly increasing computational time. In those temperature regimes, we only perform one Wolff update per step, verifying that the autocorrelation time is still acceptable. In App. A we discuss an interesting pitfall and solution we found during the implementation of the Wolff update.
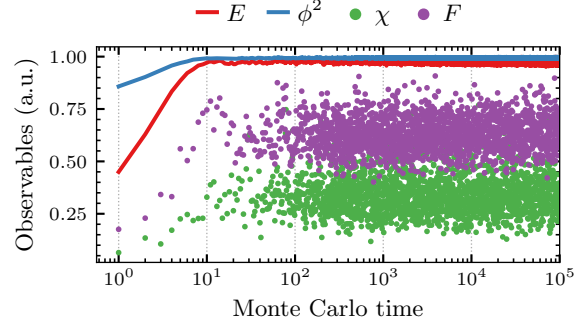
Observables

After one Monte Carlo step, we measure the magnetization density

$$\boldsymbol{m} = \frac{1}{L_\perp L_{||}^2} \left\langle \sum_i \boldsymbol{\phi}_i \right\rangle, \qquad (3.61)$$

the magnetic susceptibility

$$\chi = \frac{1}{L_\perp L_{||}^2} \left\langle \left(\sum_i \boldsymbol{\phi}_i \right)^2 \right\rangle, \qquad (3.62)$$

Fig. 3.8: Plot of the thermalization of a system. A few normalized Observables are plotted against the Monte Carlo time on a logarithmic axis.

and the Fourier transform of the correlation function at the lowest non-zero momentum

$$F = \frac{1}{L_\perp L_{||}^2} \left\langle \left| \sum_i e^{2\pi i \frac{x_i}{L_{||}}} \boldsymbol{\phi}_i \right|^2 \right\rangle, \qquad (3.63)$$

where x_i is the x-coordinate of the site i. In simulations we measure F in all periodic directions, i.e. x, y and z if z is periodic, and average the over the directions. From χ and F we calculate the second moment correlation length

$$\xi_{2\text{nd}} = \sqrt{\frac{\chi/F - 1}{4 \sin^2(\pi/L_{||})}}. \qquad (3.64)$$

For the coupling parameter method, we also measure $\Delta\mathcal{H} = \mathcal{H}_1 - \mathcal{H}_0$ as in Eq. (3.6). For the temperature integration method, we measure the internal energy density E from Eq. (3.21).

Thermalization

The first 10% of the measurements are discarded, which is more than enough to account for the thermalization of the system. This is almost certainly more than necessary, but this simple rule simplifies data analysis greatly. Fig. 3.8 shows four normalized observables on a logarithmic scale, they typically stabilize after 10^2 Monte Carlo steps. In total 10^5 steps were taken, so 10^4 values were discarded. The accuracy behaves as $\sim 1/\sqrt{\# \text{ of MC steps}}$, so the statistical uncertainty is only $\sim 5\%$ larger for 10^4 compared to 10^2.

Autocorrelation Time

When planning a Monte Carlo simulation run, the number of Monte Carlo steps between measurements is a trade off between time correlations and computational efficiency. Too few steps leads to strongly time correlated observables which wastes memory and computational time, too many steps lead to a loss of accuracy by missing unique states between measurements. The integrated autocorrelation time τ_{int} quantifies this trade-off, it is a measure of how quickly the time correlations of an observable decays to $\sim e^{-t/\tau_{\text{int}}}$ [26, Chap. 2].

In practice we use the automatic windowing algorithm [35]. The autocorrelation between the observable O_i and $O_{i+|t|}$, indexed by Monte Carlo time, is

$$\hat{C}(t) = \frac{1}{n - |t|} \sum_{i=1}^{n-|t|} (O_i - \bar{O})(O_{i+|t|} - \bar{O}), \quad (3.65)$$

where $\bar{O}$ denotes the mean of the time series and n is the total number of measurements. The normalized autocorrelation function is

$$\hat{\rho}(t) = \frac{\hat{C}(t)}{\hat{C}(0)}. \quad (3.66)$$

An example of a normalized autocorrelation function is shown in Fig. 3.9, it it unity at $t = 0$ and quickly decays with $|t|$. The integrated autocorrelation time is estimated as

$$\hat{\tau}_{\text{int}} = \frac{1}{2} \sum_{t=-n/2}^{n/2} \lambda_M(t)\hat{\rho}(t), \quad (3.67)$$

$$\lambda_M(t) = \begin{cases} 1, & |t| \leq M, \\ 0, & |t| > M, \end{cases} \quad (3.68)$$

where $\lambda_M(t)$ is a window function, that filters correlations in time longer than M. The truncation suppresses the noisy long tails of $\hat{\rho}(t)$, while preserving the dominant part of the peak in Fig. 3.9. The window length M is chosen self-consistently as the smallest number such that $M \geq 6\hat{\tau}_{\text{int}}$. Fig. 3.9 this choice would be $M = 8$. [36]

After each Monte Carlo run, the integrated autocorrelation time $\hat{\tau}_{\text{int}}$ is measured for each observable and the largest value is used as to set the binning for the Jackknife method, described below. We aimed for autocorrelation times $0.5 < \hat{\tau}_{\text{int}} < 10$.
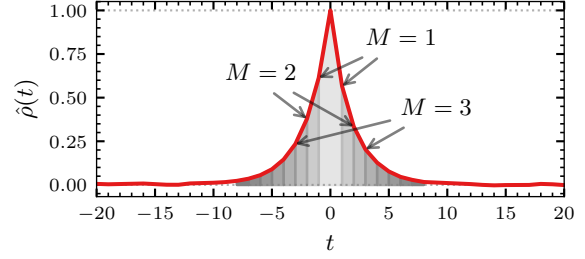
Fig. 3.9: Normalized autocorrelation function of the internal energy density E (Eq. (3.21)) of some representative simulation. The grey areas indicate the windows $\lambda_M(t)$ for $M = 1 \ldots 8$.

Jackknife Method

The expectation value of the observables is calculated with the Jackknife method. The size of the bins is set to $6\tau_{\text{int}}$. Details of the algorithm may be found in [37]. If multiple runs of the same system are available, we concatenate the binned data from all runs before applying the Jackknife method.

Scaling Variable

To see the universal behavior of the Casimir scaling function, we need to plot it against the temperature scaling variable $\bar{x}_t$. From Eq. (2.9) we have

$$\bar{x}_t = t \left(\frac{L_\perp + c}{\xi_0^+} \right)^{1/\nu}. \quad (3.69)$$

The temperature β is fixed in our simulations, so the parameters t, ν, ξ_0^+ and c have to be specified. The temperature is

$$t = \frac{\beta_c}{\beta} - 1, \quad (3.70)$$

where the critical inverse temperature β_c is accurately known, for $N = 2$ ϕ^4-model: $\beta_c = 0.508\,749\,88(6)$ at $\lambda = 2.15$ [10], for $N = 3$: ϕ^4-model $\beta_c = 0.687\,985\,21(8)$ at $\lambda = 5.2$ [11], and for $N = 4$: ϕ^4-model $\beta_c = 0.917\,875\,55(17)$ at $\lambda = 18.5$ [12].

The critical exponent ν is also well known for $N = 2$: $\nu = 0.6717(1)$ [13], for $N = 3$: ϕ^4-model $\nu = 0.711\,64(10)$ [11], and $N = 4$: ϕ^4-model $\nu = 0.748\,17(20)$ [12].

The nonuniversal amplitude ξ_0^+ of the bulk second moment correlation length ξ_{2nd} is defined as

$$\xi_{\text{2nd}}(t) = \xi_0^+ |t|^{-\nu}, \quad t > 0. \quad (3.71)$$
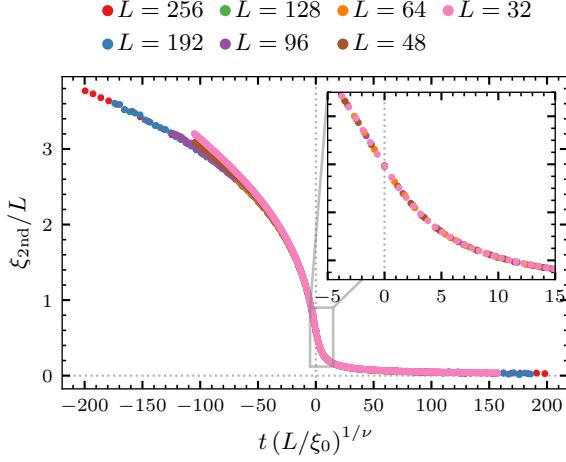
Fig. 3.10: Data collapse of the bulk second moment correlation length ξ_{2nd} for the $N = 2$ ϕ^4-model.

Fig. 3.11: Fit of Eq. (3.72) for the $N = 2$ ϕ^4-model.

	$N = 2$	$N = 3$
λ	2.15	5.2
β_c	$0.508\,749\,88(6)$	$0.687\,985\,21(8)$
ν	$0.6717(1)$	$0.711\,64(10)$
ξ_0^+	$0.4184(19)$	$0.4241(18)$

Tab. 3.5: Scaling parameters for the ϕ^4-models with $N = 2, 3$.

temperature integration method as well. Note that there might be a problem with this approach, as we observe systematic errors for the case of $\rho = 1$, in Sec. 4.2.1.
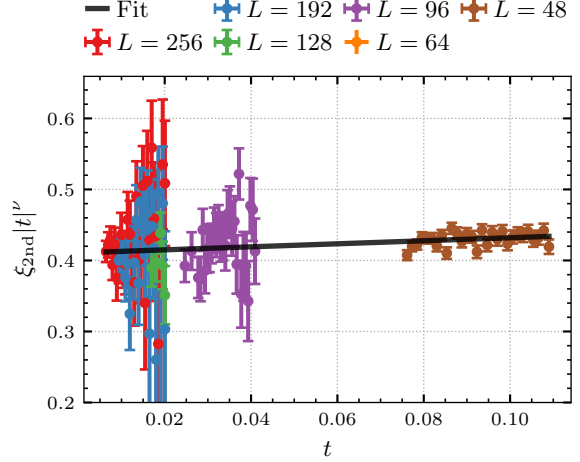
We determine ξ_0^+ with simulations of the bulk, the β ranges are summarized in Tab. 3.2. Fig. 3.10 shows a data collapse of the correlation length ξ_{2nd}/L against the scaling variable x_t, observing good agreement near criticality.

To extract ξ_0^+, we fit

$$\xi_{\mathrm{2nd}}(t)|t|^\nu = \xi_0^+(1 + bt), \qquad (3.72)$$

where b is an analytic correction. Note that a more in-depth application of this method can be found in [38]. The fit in Eq. (3.72) is valid for $\xi_{\mathrm{2nd}} \ll L$, conservatively we choose $\xi_{\mathrm{2nd}}/L < 1/20$ and fit across all available lattice sizes. An example fit is shown in Fig. 3.11. For the $N = 2$ we get $\xi_0^+ = 0.4184(19)$, $b = 0.298(26)$, and $\chi^2/\mathrm{dof} = 1.22(11)$. For the $N = 3$ we get $\xi_0^+ = 0.4241(18)$, $b = 0.28(4)$, and $\chi^2/\mathrm{dof} = 1.02(15)$. Tab. 3.5 summarizes the scaling parameters used in the next chapter.

Finally, the correction to the thickness c in Eq. (3.69) is the same in the coupling parameter and the temperature integration method. We determine c by fitting Eq. (3.16) for specific ρ and boundary conditions, and use this value it in the

Chapter 4

Results

In this chapter we present Monte Carlo results for the critical Casimir force in the ϕ^4-model for various boundary conditions and universality classes. We first analyze the Casimir amplitude at criticality in Sec. 4.1 and the full Casimir scaling function in Sec. 4.2.

4.1 Casimir Amplitude

In this section we investigate the behavior of the critical Casimir amplitude θ at the critical point $\beta = \beta_c$ in the ϕ^4-model for various boundary conditions.

In literature, the focus is mostly on the Casimir force in film geometries, meaning $\rho \to 0$, partly as for comparison with experiments. However, the aspect ratio ρ is a valid and interesting scaling variable and has been investigated as such in [8, 6]. Here we focus on two cases, $\rho = 1$, we call *cube geometry*, and $\rho = 1/4$, we call *film geometry*. The latter is chosen as a compromise between computational cost and convergence to the true film geometry $\rho \to 0$. We will see that $\rho = 1/4$ captures the essential features of the Casimir force in the film geometry. Note, in the following sections we quote $\rho = (L_\perp - 1)/L_{||}$, which is different from the true aspect ratio $\tilde{\rho} = (L_\perp - 1/2)/L_{||}$ defined in Eq. (3.17), the comparison of the cube and film geometry is only qualitative.

The boundary conditions also greatly influence the Casimir force. With either surface fields $\boldsymbol{h}_{\text{top}}$ and $\boldsymbol{h}_{\text{bottom}}$ or surface enhancements β_s, a diverse behavior of the Casimir force is observed. If one non-zero field is present the surface flows to the normal universality class, which is represented by $+$ or $-$, the ordinary and extraordinary universality classes are represented by o and e, respectively.

Combinations of boundary conditions are denoted by a tuple such as (o, o), (e, o), $(+, o)$, etc., with arbitrary order. If both surfaces are in the normal universality class, only the relative angle $\alpha \in [0, \pi]$ between the fields is relevant, so the systems are denoted with α.

4.1.1 (o, o) Boundary Conditions

Ordinary boundary conditions (o, o), so no external fields $\boldsymbol{h}_{\text{top}} = \boldsymbol{h}_{\text{bottom}} = 0$ and no surface enhancements $\beta_s = \beta$, are the most widely studied, including experimental realization [4]. In the experiment it is an attractive Casimir force is observed in a thin film of He^4 ($O(2)$ universality class).

Tab. 4.1 shows fits of Eq. (3.16) for $N = 2, 3$ in cube ($\rho = 1$) and film geometry ($\rho = 1/4$). In film geometry the Casimir amplitude is negative implying an attractive Casimir force, consistent with experiment. In true film geometry ($\rho \to 0$) for $N = 2$, $\theta = -0.060(2)$ [39], slightly smaller than our result $\theta = -0.050(7)$. In contrast, for cube geometry, we find a large positive Casimir amplitude. For the XY-model the Casimir amplitude appears to be monotonically increasing over $0 \lesssim \rho \lesssim 1$ from $\theta = -0.060(2)$ to $\theta = 0.592(32)$. For the Heisenberg model, we do not know of results for $\rho \to 0$, but it is reasonable to assume a similar increase with ρ.

For the Ising model with fully periodic boundary conditions, renormalization-group calculations [8] and Monte Carlo simulations [6] show the same trend with ρ in $N = 1$. Particularly, for $\rho < 1$ the Casimir force is attractive, for $\rho > 1$ repulsive, and for $\rho = 1$ vanishes.

Furthermore, $|\theta|$ grows with N, more about this below in Sec. 4.1.4.

			θ	c	B	χ^2/dof
(o,o)	$\rho=1$	$N=1$ [40]	$0.301(4)$			
		$N=2$	$0.592(32)$	$0.29(15)$	$0.163\,412\,5(18)$	$1.5(8)$
		$N=3$	$0.935(31)$	$0.42(9)$	$0.261\,585\,8(16)$	$1.6(8)$
	$\rho=1/4$	$N=2$	$-0.050(7)$	$0.5(4)$	$0.163\,411\,4(9)$	$0.7(8)$
		$N=3$	$-0.073(11)$	$0.6(4)$	$0.261\,588\,5(14)$	$1.2(8)$
$(+,o)$	$\rho=1$	$N=1$ [40]	$0.601(4)$			
		$N=2$	$0.84(4)$	$0.53(16)$	$0.163\,411\,4(30)$	$0.8(7)$
		$N=3$	$1.15(4)$	$0.55(9)$	$0.261\,587\,6(19)$	$0.4(8)$
		$N=4$	$1.41(4)$	$0.44(8)$	$0.368\,010\,1(23)$	$0.7(8)$
	$\rho=1/4$	$N=2$	$0.520(24)$	$0.89(13)$	$0.163\,411\,4(23)$	$0.4(10)$
		$N=3$	$0.574(29)$	$0.87(14)$	$0.261\,590\,9(27)$	$0.2(10)$
		$N=4$	$0.67(4)$	$0.03(16)$	$0.368\,011\,4(33)$	$0.4(10)$
(e,o)	$\rho=1$	$N=2$ ($\beta_s=2.5\beta$)	$0.93(4)$	$-0.28(9)$	$0.163\,412\,8(15)$	$1.3(8)$
		$N=3$ ($\beta_s=3\beta$)	$1.16(5)$	$-0.33(11)$	$0.261\,590\,1(15)$	$0.9(8)$
		$N=4$ ($\beta_s=5.5\beta$)	$1.42(6)$	$-0.33(13)$	$0.368\,018\,8(33)$	$2.2(7)$

Tab. 4.1: Casimir amplitude θ for (o,o), $(+,o)$, and (e,o) boundary conditions in the ϕ^4-model. We also include $\rho=1$, $N=1$ from [40]. Note the parentheses in χ^2/dof indicate the square root of the variance $\sqrt{2/dof}$.

4.1.2 $(+,o)$ Boundary Conditions

Systems with $(+,o)$ boundary conditions have one symmetry breaking surface field and one ordinary surface, w.l.o.g. $\boldsymbol{h}_{\mathrm{top}}=0$ and $\boldsymbol{h}_{\mathrm{bottom}}\neq 0$, and no surface enhancements $\beta_s=\beta$.

Tab. 4.1 shows the results of the fits, similarly to the (o,o), we observe larger Casimir amplitudes as ρ increases and larger $|\theta|$ as N increases. In contrast to (o,o), the Casimir amplitude is completely positive for $(+,o)$, implying the Casimir force is always repulsive. For the identical ρ and N, the Casimir amplitude of $(+,o)$ is always larger compared to (o,o), so the symmetry breaking field on one surface makes the the force more repulsive. This is consistent with the Ising universality class in the true film geometry, the Casimir amplitude for $(+,o)$ is $\theta=0.492(5)$ versus $\theta=-0.030(2)$ for (o,o) [5].

4.1.3 (e,o) Boundary Conditions

The extraordinary surface universality class is realized by setting the surface field to zero $\boldsymbol{h}_{\mathrm{top}}=0$, and introducing a strong surface enhancement $\beta_s>\beta$. We chose $\beta_s=2.5\beta$ for $N=2$, $\beta_s=3\beta$ for $N=3$, and $\beta_s=5.5\beta$ for $N=4$, following [41].

In [42], the extraordinary surface universality class is investigated with conformal field theory and renormalization-group arguments. The surface is described by a non-linear σ-model with surface coupling $\sim 1/g$. It is argued, that in the presence of a critical bulk, the coupling g flows logarithmically to zero, the *extraordinary-log* fixed point. This is supported by Monte Carlo simulations [41]. At the fixed point, the surface "almost" orders, with the correlation function decaying as $\sim 1/\log(x)^q$. It is expected, that the Casimir force of (e,o) is the same as in $(+,o)$. Due to the logarithmic flow of the extraordinary phase, the Casimir amplitude collects a logarithmic scaling correction. For (e,o) fits we replaced the $1/L_\perp$ scaling correction in Eq. (3.16) by a $1/\ln(L_\perp)$ correction

$$I(\beta, L_\perp, L_{||}) = B(t) + \frac{[\theta\,(\tilde{x}_t, \tilde{\rho}) + c/\ln(L_\perp - 1/2)]}{(L_\perp - 1/2)^3}. \tag{4.1}$$

In principle the $1/L_\perp$ term is still present, but the logarithmic correction dominates. Tab. 4.1 shows the (e,o) fits at $\rho=1$. The Casimir amplitudes are consistent with those for $(+,o)$, this supports the theory behind the extraordinary-log fixed point.

4.1.4 Continuous α Boundary Conditions

We now consider two surfaces in the normal universality class, that is, both surfaces have symmetry
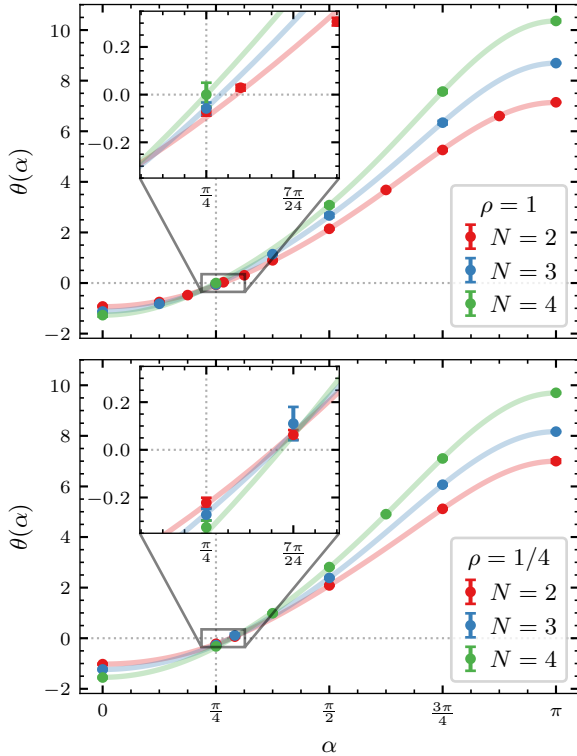
Fig. 4.1: Casimir amplitude θ as a function of the relative field angle α. **Top:** $\rho = 1$, $N = 2, 3, 4$. **Bottom:** $\rho = 1/4$, $N = 2, 3, 4$. Semi-transparent lines are guides to the eye from truncated Fourier fits. Insets show the approximate area of the roots.

breaking fields $\boldsymbol{h}_{\text{top}} \neq 0$ and $\boldsymbol{h}_{\text{bottom}} \neq 0$. We determine θ at criticality as a function of the relative angle α between the surface fields. We expect the function $\theta(\alpha)$ to be periodic with period 2π and symmetric around the points $\alpha = \pi n$, $n \in \mathbb{Z}$, so the entire curve can be reconstructed from the interval $\alpha \in [0, \pi]$.

Fig. 4.1 shows the Casimir amplitude for $\rho = 1$ and $\rho = 1/4$ with $N = 2, 3, 4$. The semi-transparent lines are guides to the eye attained from low order Fourier fits and do not represent the exact shape of $\theta(\alpha)$.

We observe that the Casimir amplitude θ is minimal at $\alpha = 0$ and maximal at $\alpha = \pi$. This makes physical sense, at $\alpha = 0$ the external fields are aligned and attract each other, while at $\alpha = \pi$ the anti-aligned fields produce a repulsive Casimir force. We see that the repulsion $\theta(\pi) \sim 6 \dots 9$ is much stronger than the attraction $\theta(0) \sim -2 \dots -1$,

for both cube and film geometry. For larger N the Casimir force is stronger, mirroring the trend observed in (o, o) and $(+, o)$.

The $\theta(\alpha)$ curves for different N have a similar shape and appear to differ mainly by a scaling factor for the respective ρ's. If they do differ by just a scaling factor, the roots of the curves must coincide. The insets of Fig. 4.1 show the approximate area of the roots $\theta(\alpha_0) = 0$. For $\rho = 1$, the roots lie near $\alpha_0 \approx \pi/4$, with the current precision it is inconclusive, whether the roots coincide for the different N. For $\rho = 1/4$, the roots are consistent with a common value slightly below $\alpha_0 \approx 7\pi/24$. Clearly, α_0 depends on the aspect ratio ρ. To our knowledge, there is no prediction in literature for α_0 as $\rho \to 0$ or for the limit $N \to \infty$, both would be interesting to investigate.

Mean-field results for the XY-model in the true film geometry $\rho \to 0$ [9, 43] show a qualitatively similar behavior to Fig. 4.1. $\theta(\alpha)$ goes from negative at $\alpha = 0$ to positive at $\alpha = \pi$, but the position of the root in mean-field theory is at $\pi/3$, which is not compatible with our result $\alpha_0 \approx 7\pi/24$ for $\rho = 1/4$.

4.2 Casimir Scaling Function

In this section we investigate the critical Casimir scaling function θ as a function of the temperature scaling variable x_t for various boundary conditions. In the last section we determined the Casimir amplitude θ at criticality, but the Casimir force exhibits interesting behavior in a whole temperature range around criticality $x_t \neq 0$. At high temperatures it is strongly suppressed away from criticality, but persists as long as $\xi \gtrsim L_\perp$. At low temperatures the system orders, and the limiting behavior as $x_t \to -\infty$ depends on the boundary conditions. The shape of $\theta(x_t)$ is non-trivial and depends on the boundary conditions, the universality class, and the aspect ratio ρ. For $N = 2$, (o, o), and $\rho \to 0$ the shape of $\theta(x_t)$ is well known from simulations and experiments. [7, 24, 4, 44]

Mean-field calculations for surfaces in the normal universality class predict $\theta(x_t)$ for $N = 2$ in the true film geometry $\rho \to 0$ as a function of α [9]. In particular, at $\alpha = \pi$ the scaling function develops a kink at a temperature below criticality, which has not yet been reproduced by simulations.
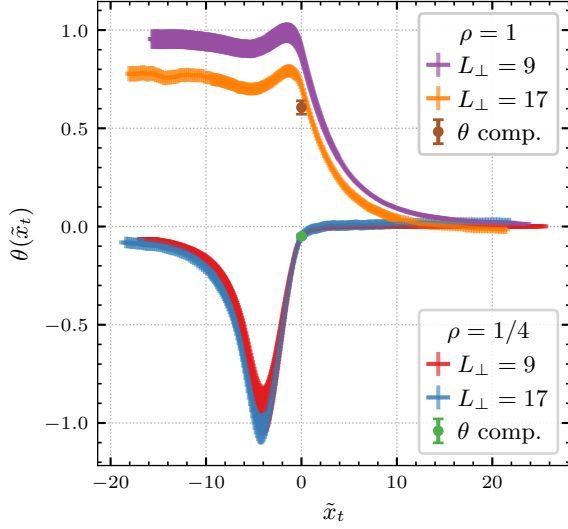
Fig. 4.2: Casimir scaling function θ for $N = 2$ and (o, o) as a function of x_t. Cube and film geometries are shown for multiple lattice sizes. The Casimir amplitudes θ from the coupling method in Sec. 3.2.1 are included for comparison.
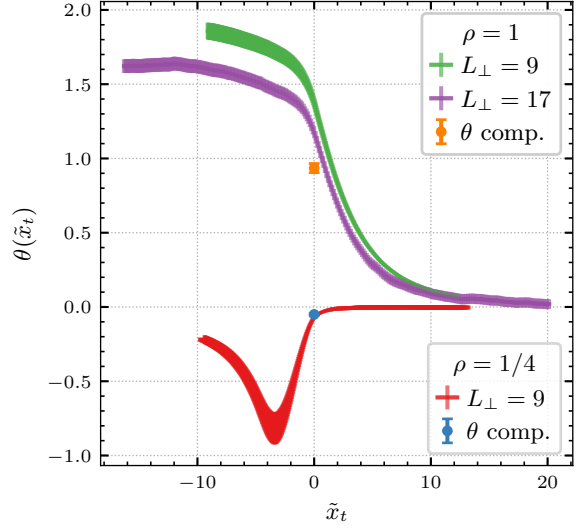

Fig. 4.3: Same as Fig. 4.2 for $N = 3$.

4.2.1 (o, o) Boundary Conditions

We first discuss the Casimir scaling function $\theta(x_t)$ for (o, o) boundary conditions. Fig. 4.2 and 4.3 show results for $N = 2$ and $N = 3$ for cube and film geometries.

Film Geometry

For the XY-model with $\rho = 1/4$, shown in Fig. 4.2, the $L_\perp = 9$ and $L_\perp = 17$ curves agree within error bars, which means the approximations in our method are valid down to at least $L_\perp = 9$ in this case. At criticality, $\tilde{x}_t = 0$, the result from the coupling parameter method in Tab. 4.1 is plotted as a single point, the two methods are in good agreement. Note that the integration method uses c obtained from the coupling parameter method, so they are not completely independent, nevertheless this consistency check is non-trivial.

In true film geometry $\rho \to 0$, $\theta(\tilde{x}_t)$ is is well established, at high temperatures it goes to zero and at low temperature it approaches $\theta(-\infty) \approx -0.047\,83$ [44], consistent with our simulation. In Fig. 4.2 the minimum is around $(x_{\min}, \theta_{\min}) = (-4, -1)$. For the true film geometry, the minimum is $(x_{\min}, \theta_{\min}) = (-4.95(3), -1.31(3))$ [44]. The small discrepancy is expected, as $\rho = 1/4$ is not quite converged to the true film geometry.

For the Heisenberg model, shown in Fig. 4.3, the overall shape matches that of the XY-model, and agrees with the coupling parameter method (see Tab. 4.1) at the criticality. To our knowledge, the Casimir scaling function for $N = 3$ has not yet been published.

Cube Geometry

For the XY-model with $\rho = 1$, shown in Fig. 4.2, the curves for $L_\perp = 9$ and $L_\perp = 17$ are presented. At high temperatures, θ goes to zero, but not as quickly as in the film geometry. For the entire range the Casimir scaling function remains completely positive. At low temperatures, θ approaches a constant positive value, however there is significant disagreement between the lattice sizes. Both sizes have a local maximum around $\tilde{x}_t \approx -2$, followed by a local minimum around $\tilde{x}_t \approx -5$, conceivably a remnant of the minimum in film geometry. For fully periodic boundary conditions, the minimum moves similarly as a function of ρ [8, 6]. Unfortunately, the temperature integration method also significantly deviates from the coupling parameter method at criticality.

For the Heisenberg-model, shown in Fig. 4.3, the curves for $L_\perp = 9$ and $L_\perp = 17$ are presented as well. The curves are also completely positive, vanish at high temperatures, and seem to converge to a
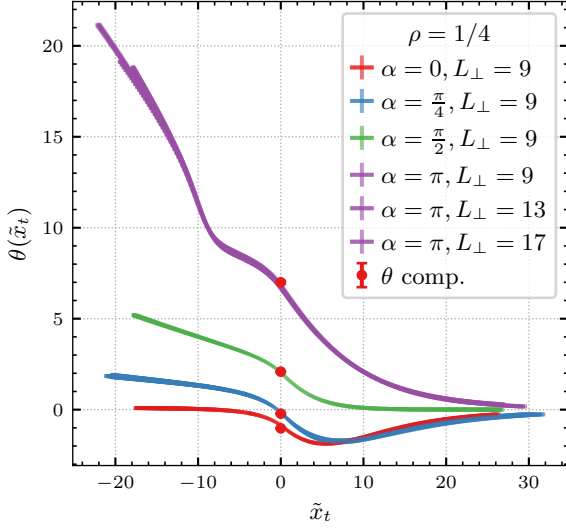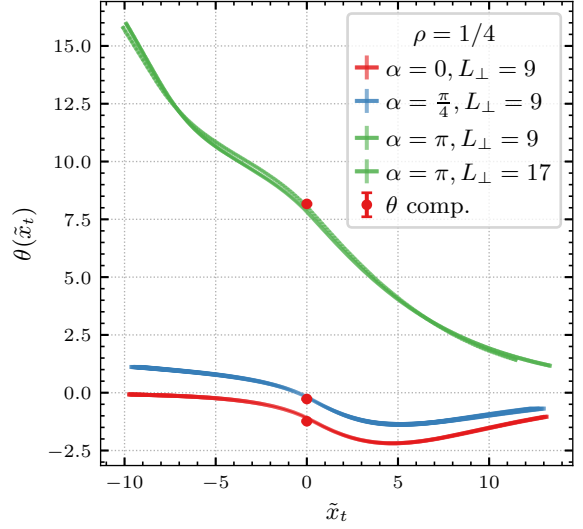
Fig. 4.4: Casimir scaling function θ for $N = 2$ in the film geometry at several α, as a function of x_t. The θ values from the coupling method in the previous section are shown as well.

Fig. 4.5: Same as Fig. 4.4 for $N = 3$.

positive value at low temperatures. In contrast to the XY-model, the curves do not show a local maximum or minimum near criticality, rather they decrease monotonically. They do show a reduced slope around $\tilde{x}_t \approx -4$, possibly a remnant of the minimum of the film geometry.

For both $N = 2$ and $N = 3$, the curves for $L_\perp = 9$ lie above $L_\perp = 17$, which in turn lie above θ from the coupling parameter method. This indicates a systematic error specific to $\rho = 1$, which we have not yet fully identified. It seems most likely that the scaling correction c is responsible for this discrepancy, as it is also a function of ρ. More careful checking of the $1/L_\perp$ correction with the coupling parameter method away from criticality may bring clarity.

4.2.2 Continuous α Boundary Conditions

Next, we apply external fields to both surfaces and study how the Casimir scaling function changes with the relative angle α between the fields. Figs. 4.4 and 4.5 show results for $N = 2$ and $N = 3$ for various α. We see that the Casimir amplitudes have diverse shapes as a function of x_t. Only the film geometry is investigated in this subsection.

Fig. 4.4 shows Monte Carlo results for the XY-model with $\alpha = 0, \frac{\pi}{4}, \frac{\pi}{2}, \pi$, together with the Casimir amplitudes from the coupling parameter method in Fig. 4.1. At high temperatures, all curves go to zero and at criticality the curves agree with the coupling parameter method. At low temperatures, the curves with $\alpha > 0$ seem to diverge to $+\infty$, with larger α diverging more strongly. In contrast, with $\alpha = 0$, $\theta(\tilde{x}_t)$ converges to zero or some small negative value. Depending on α and $\tilde{x}_t$, the Casimir force can be repulsive or attractive, for most α the curve crosses zero at some temperature $\theta(\tilde{x}_{t,0}) = 0$. For small α the root is at low temperatures $\tilde{x}_{t,0} < 0$, for larger α the root moves to higher temperatures. At around $\alpha \approx \pi/4$ the root passes through criticality $\tilde{x}_{t,0} = 0$. This is consistent with the coupling parameter method, where the root is at $\alpha_0 \approx 7\pi/24$, as shown in the bottom panel of Fig. 4.1.

In Fig. 4.6 we overlay our Monte Carlo results with rescaled mean-field results from [9]. After rescaling the mean-field curves, such that they match the Monte Carlo results best, the qualitative correspondence is striking. However, mean-field theory predicts a critical root $(\tilde{x}_t, \theta) = (0, 0)$ at $\alpha_0 = \pi/3$, whereas our Monte Carlo curve crosses at around $\alpha_0 \approx 7\pi/24$, this discrepancy can not be accounted for by rescaling.

Fig. 4.5 shows the Heisenberg-model, the curves agree with the Casimir amplitudes from Fig. 4.1, and have a similar behavior to the XY-model. They
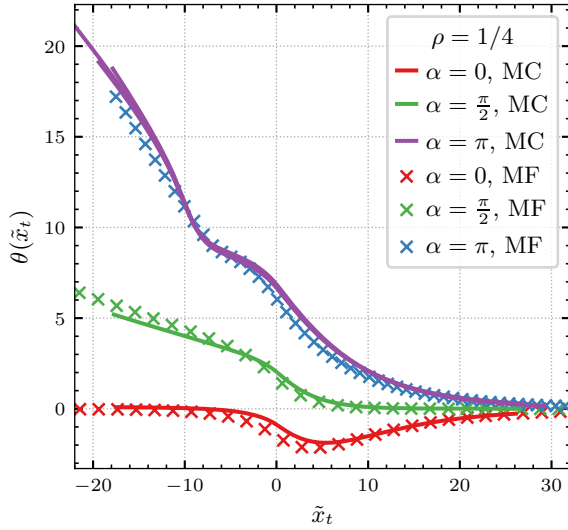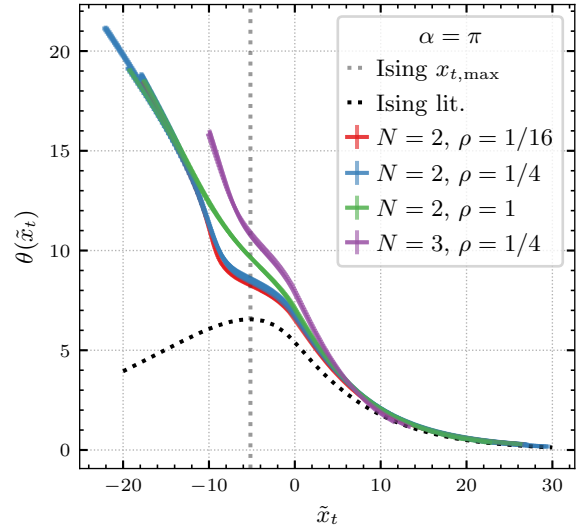
Fig. 4.6: Monte Carlo (MC) curves from Fig. 4.4, overlaid with rescaled mean-field (MF) results from [9].

Fig. 4.7: Casimir scaling function θ for $N = 2$ and $N = 3$ in film geometry with $\alpha = \pi$. The dotted curve shows the Ising Casimir scaling function from [46], the dotted vertical line at $x_t = -5.17(7)$ marks its maximum.

go to zero at high temperatures and diverge at low temperatures limit for $\alpha > 0$. To our knowledge, there are no mean-field results available for the Heisenberg-model.

The Kink

An additional feature seen in the mean-field analysis is a non-differentiable *kink* in $\theta(\tilde{x}_t)$ for $\alpha = \pi$. In Figs. 4.4 and 4.5 we also observe a sudden change in slope for $\alpha = \pi$.

In mean-field theory, the kink emerges from a spontaneous breaking of symmetry. There are two competing magnetization profiles in the film, (i) a linear interpolation between the two surfaces, where the magnetization goes to zero in the middle of the film, and (ii) a rotational profile, where the magnetization twists by 180° from one surface to the other, keeping its magnitude constant. (In [9] the two options are visualized in Fig. 1). At low temperatures, the twisting is energetically favorable, while at high temperatures, the linear interpolation wins. The kink appears at the temperature where the two options are equal in energy. The rotational state has two degenerate minima, either the magnetization profile rotates clockwise or counter-clockwise. Coming from high temperatures the symmetry is spontaneously broken in the rotational state, resulting in non-differentiable behavior of $\theta(\tilde{x}_t)$. Above

the kink temperature (case (i)), the Casimir scaling function of the XY-model is identical to that of the Ising model (Plotted in Fig. 3 of [9]). The kink in the XY-model is exactly at the position where the Ising model has its maximum [45].

Fig. 4.7 shows the XY-model curves for $\alpha = \pi$ with $\rho = 1, \frac{1}{4}, \frac{1}{16}$ and several lattice sizes. The kink is barely visible for $\rho = 1$, becomes more pronounced at $\rho = 1/4$, and sharpens further for $\rho = 1/16$. We also show the Ising Casimir scaling function from [46] as a black dotted curve, the dotted vertical line at $x_t = -5.17(7)$ marks its maximum. The XY- and Ising-model are close at high temperatures but separate below $\tilde{x}_t = 10$. In contrast to mean-field theory, they do not coincide at the Ising maximum. Nevertheless the temperature of the kink is close to the Ising maximum.

Fig. 4.5 also shows the $N = 3$ curve with $\alpha = \pi$ and $\rho = 1/4$, a kink is visible, although less pronounced than in $N = 2$. This is consistent with the additional magnetic degree of freedom softening the kink. The temperature of the kink is similar to that of the XY-model and Ising maximum.

Future work could investigate the kink in more detail by measuring the magnetization profile in the film.

24

Chapter 5

Conclusion

In this thesis we have studied the critical Casimir force in three-dimensional $O(N)$-models, focusing on a range of boundary conditions and system geometries. By systematically varying the aspect ratio, surface fields, and surface enhancements, we explored the rich phenomenology of the Casimir effect beyond the well-studied Ising universality class.

We focused on $N = 2, 3, 4$, reproducing known results for the Casimir amplitude and extending them to new boundary conditions and geometries. In particular, we studied combinations of ordinary, extraordinary, and normal surface universality classes. We replicated the recently found logarithmic RG-flow from the extraordinary to the normal surface universality class. We also examined the continuous α boundary conditions, which interpolate between the well-known $(+,+)$ and $(+,-)$ boundary conditions. We found that the Casimir force vanishes for some angle α_0, which is dependent on the N and the aspect ratio ρ. The precise angle and nature of this root is an interesting avenue for future research, analytical calculations may be feasible in the large-N or $\rho \to 0$ limits.

Using the temperature integration method, we studied the Casimir scaling function for temperatures close to the phase transitions of the bulk. We could replicate well-known scaling functions for the XY-model and extend them to the Heisenberg-model and normal boundary conditions. The scaling functions show a diverse behavior, with a rich structure of extrema, that depend on the boundary conditions and the aspect ratio ρ. Comparison with mean-field calculations for $N = 2$ shows qualitative agreement. A predicted kink from mean-field theory in the scaling function for two surface fields with relative angle $\alpha = \pi$ is observed in our Monte Carlo results, moreover it is preserved in $N = 3$.

We developed and implemented efficient and flexible Monte Carlo algorithms, combining cluster and local updates, adaptable to different N and boundary conditions. High precision results for the Casimir amplitude and scaling function were obtained, with the coupling parameter and temperature integration methods, respectively.

Looking ahead, several promising directions for future research could be pursued. The nature of the root of the Casimir amplitude for α boundary conditions could be studied in more detail, especially the dependence on N and ρ. A study of the magnetization profiles in the film for $\alpha = \pi$ could shed light on the nature of the kink in the scaling function, and its dependence on N. Explaining the inconsistency in the scaling functions for different lattice sizes at $\rho = 1$ is the most pressing open problem.

Overall, this thesis has contributed to a deeper understanding of the critical Casimir force in $O(N)$-models, revealing new phenomena and providing a foundation for future numerical and analytical investigations.

Acknowledgements

Bibliography

[1] C. Hertlein et al. "Direct measurement of critical Casimir forces". In: *Nature* 451.7175 (Jan. 2008), pp. 172–175. ISSN: 1476-4687. DOI: 10.1038/nature06443.

[2] A. Gambassi and S. Dietrich. "Critical Casimir forces in soft matter". In: *Soft Matter* 20.15 (2024), pp. 3212–3242. ISSN: 1744-6848. DOI: 10.1039/d3sm01408h.

[3] John Cardy. *Scaling and renormalization in statistical physics*. Cambridge lecture notes in physics 5. Cambridge: Cambridge University Press, 1996. 1238 pp. ISBN: 9781316036440.

[4] A. Ganshin et al. "Critical Casimir Force in ^{4}He Films: Confirmation of Finite-Size Scaling". In: *Phys. Rev. Lett.* 97 (7 Aug. 2006), p. 075301. DOI: 10.1103/PhysRevLett.97.075301. URL: https://link.aps.org/doi/10.1103/PhysRevLett.97.075301.

[5] Francesco Parisen Toldin, Matthias Tröndle, and S. Dietrich. "Critical Casimir forces between homogeneous and chemically striped surfaces". In: *Physical Review E* 88.5 (Nov. 2013), p. 052110. ISSN: 1550-2376. DOI: 10.1103/physreve.88.052110.

[6] Alfred Hucht, Daniel Grüneberg, and Felix M. Schmidt. "Aspect-ratio dependence of thermodynamic Casimir forces". In: *Physical Review E* 83.5 (May 2011), p. 051101. ISSN: 1550-2376. DOI: 10.1103/physreve.83.051101.

[7] O. Vasilyev et al. "Monte Carlo simulation results for critical Casimir forces". In: *Europhysics Letters (EPL)* 80.6 (Nov. 2007), p. 60009. ISSN: 1286-4854. DOI: 10.1209/0295-5075/80/60009.

[8] V. Dohm. "Critical Casimir force in slab geometry with finite aspect ratio: Analytic calculation above and below T_c". In: *EPL (Europhysics Letters)* 86.2 (Apr. 2009), p. 20001. ISSN: 1286-4854. DOI: 10.1209/0295-5075/86/20001.

[9] Jonathan Bergknoff, Daniel Dantchev, and Joseph Rudnick. "Casimir force in the rotor model with twisted boundary conditions". In: *Physical Review E* 84.4 (Oct. 2011), p. 041134. ISSN: 1550-2376. DOI: 10.1103/physreve.84.041134.

[10] Francesco Parisen Toldin. "Finite-size scaling at fixed renormalization-group invariant". In: *Physical Review E* 105.3 (Mar. 2022), p. 034137. ISSN: 2470-0053. DOI: 10.1103/physreve.105.034137.

[11] Martin Hasenbusch. "Monte Carlo study of a generalized icosahedral model on the simple cubic lattice". In: *Physical Review B* 102.2 (July 2020), p. 024406. ISSN: 2469-9969. DOI: 10.1103/physrevb.102.024406.

[12] Martin Hasenbusch. "Three-dimensional $O(N)$-invariant ϕ^4 models at criticality for $N \geq 4$". In: *Physical Review B* 105.5 (Feb. 2022), p. 054428. ISSN: 2469-9969. DOI: 10.1103/physrevb.105.054428.

[13] Massimo Campostrini et al. "Theoretical estimates of the critical exponents of the superfluid transition in ^{4}He by lattice methods". In: *Physical Review B* 74.14 (Oct. 2006), p. 144506. ISSN: 1550-235X. DOI: 10.1103/physrevb.74.144506.

[14] Kurt Binder. "Critical Behaviour at Surfaces". In: *Phase transitions and critical phenomena*. Ed. by Cyril Domb, M. S. Green, and J. L. Lebowitz. 2. print. Vol. Vol. 8. London [u.a.]: Acad. Press, 1989. ISBN: 0122203089.

[15] H. B. G. Casimir. "On the attraction between two perfectly conducting plates". In: *Indag. Math.* 10.4 (1948), pp. 261–263.

[16] M. E. Fisher and P.-G. de Gennes. "Phénomènes aux parois dans un mélange binaire critique". In: *C. R. Acad. Sc. Paris.* B 287 (1978), pp. 207–209.

[17] F. Parisen Toldin. "Surface critical behavior of the three-dimensional O(3) model". In: *Journal of Physics: Conference Series* 2207.1 (Mar. 2022), p. 012003. ISSN: 1742-6596. DOI: 10.1088/1742-6596/2207/1/012003.

[18] Vladimir Privman. "Finite-Size Scaling Theory". In: *Finite size scaling and numerical simulation of statistical systems.* Ed. by Vladimir Privman. Singapore: World Scientific, 1990. ISBN: 9789813208766.

[19] T. Weston Capehart and Michael E. Fisher. "Susceptibility scaling functions for ferromagnetic Ising films". In: *Physical Review B* 13.11 (June 1976), pp. 5021–5038. ISSN: 0556-2805. DOI: 10.1103/physrevb.13.5021.

[20] Francesco Parisen Toldin and S. Dietrich. "Critical Casimir forces and adsorption profiles in the presence of a chemically structured substrate". In: *Journal of Statistical Mechanics: Theory and Experiment* 2010.11 (Nov. 2010), P11003. ISSN: 1742-5468. DOI: 10.1088/1742-5468/2010/11/p11003.

[21] M. Hasenbusch and T. Török. "High-precision Monte Carlo study of the 3DXY-universality class". In: *Journal of Physics A: Mathematical and General* 32.36 (Aug. 1999), pp. 6361–6371. ISSN: 1361-6447. DOI: 10.1088/0305-4470/32/36/301.

[22] K. K. Mon. "Monte Carlo studies of critical free energies and the simple-cubic Ising model". In: *Physical Review B* 39.1 (Jan. 1989), pp. 467–470. ISSN: 0163-1829. DOI: 10.1103/physrevb.39.467.

[23] A. S. Kronrod. "Integration with control of accuracy". In: *Dokl. Akad. Nauk SSSR* 154.2 (1964), pp. 283–286. URL: http://mi.mathnet.ru/dan29027.

[24] Alfred Hucht. "Thermodynamic Casimir Effect in ^{4}He Films near T_λ: Monte Carlo Results". In: *Phys. Rev. Lett.* 99 (18 Nov. 2007), p. 185301. DOI: 10.1103/PhysRevLett.99.185301. URL: https://link.aps.org/doi/10.1103/PhysRevLett.99.185301.

[25] William H. Press, ed. *Numerical recipes. The art of scientific computing.* 3. ed. Cambridge [u.a.]: Cambridge University Press, 2007. 1235 pp. ISBN: 0521880688.

[26] David P. Landau. *A guide to Monte Carlo simulations in statistical physics.* Ed. by Kurt Binder. Fourth edition. Title from publisher's bibliographic system (viewed on 05 Oct 2015). Cambridge: Cambridge University Press, 2015. 1519 pp. ISBN: 9781139696463.

[27] Kurt Binder. "Monte Carlo Investigations of Phase Transitions and Critical Phenomena". In: *Phase transitions and critical phenomena.* Ed. by Cyril Domb, M. S. Green, and J. L. Lebowitz. Vol. Vol. 5B. London [u.a.]: Acad. Press, 1976. ISBN: 0122203054.

[28] Nicholas Metropolis et al. "Equation of State Calculations by Fast Computing Machines". In: *The Journal of Chemical Physics* 21.6 (June 1953), pp. 1087–1092. ISSN: 1089-7690. DOI: 10.1063/1.1699114.

[29] Stephen L. Adler. "Over-relaxation method for the Monte Carlo evaluation of the partition function for multiquadratic actions". In: *Physical Review D* 23.12 (June 1981), pp. 2901–2904. ISSN: 0556-2821. DOI: 10.1103/physrevd.23.2901.

[30] Francesco Parisen Toldin. "Boundary Critical Behavior of the Three-Dimensional Heisenberg Universality Class". In: *Physical Review Letters* 126.13 (Mar. 2021), p. 135701. ISSN: 1079-7114. DOI: 10.1103/physrevlett.126.135701.

[31] C. M. Fortuin and P. W. Kasteleyn. "On the random-cluster model". In: *Physica* 57.4 (Feb. 1972), pp. 536–564. ISSN: 0031-8914. DOI: 10.1016/0031-8914(72)90045-6.

[32] Robert H. Swendsen and Jian-Sheng Wang. "Nonuniversal critical dynamics in Monte Carlo simulations". In: *Physical Review Letters* 58.2 (Jan. 1987), pp. 86–88. ISSN: 0031-9007. DOI: 10.1103/physrevlett.58.86.

[33] Ulli Wolff. "Collective Monte Carlo Updating for Spin Systems". In: *Physical Review Letters* 62.4 (Jan. 1989), pp. 361–364. ISSN: 0031-9007. DOI: 10.1103/physrevlett.62.361.

[34] Jaron Kent-Dobias and James P. Sethna. "Cluster representations and the Wolff algorithm in arbitrary external fields". In: *Physical Review E* 98.6 (Dec. 2018), p. 063306. ISSN: 2470-0053. DOI: `10.1103/physreve.98.063306`.

[35] S. Caracciolo and A. D. Sokal. "Dynamic critical exponent of some Monte Carlo algorithms for the self-avoiding walk". In: *Journal of Physics A: Mathematical and General* 19.13 (Sept. 1986), pp. L797–L805. ISSN: 1361-6447. DOI: `10.1088/0305-4470/19/13/008`.

[36] Neal Madras and Alan D. Sokal. "The pivot algorithm: A highly efficient Monte Carlo method for the self-avoiding walk". In: *Journal of Statistical Physics* 50.1–2 (Jan. 1988), pp. 109–186. ISSN: 1572-9613. DOI: `10.1007/bf01022990`.

[37] Peter Young. *Everything You Wanted to Know about Data Analysis and Fitting but Were Afraid to Ask*. SpringerBriefs in Physics Ser. Description based on publisher supplied metadata and other sources. Cham: Springer International Publishing AG, 2015. 188 pp. ISBN: 9783319190518. DOI: `10.1007/978-3-319-19051-8`.

[38] Martin Hasenbusch. "The Kosterlitz–Thouless transition in thin films: a Monte Carlo study of three-dimensional lattice models". In: *Journal of Statistical Mechanics: Theory and Experiment* 2009.02 (Feb. 2009), P02005. ISSN: 1742-5468. DOI: `10.1088/1742-5468/2009/02/p02005`.

[39] Martin Hasenbusch. "Another method to compute the thermodynamic Casimir force in lattice models". In: *Physical Review E* 80.6 (Dec. 2009), p. 061120. ISSN: 1550-2376. DOI: `10.1103/physreve.80.061120`.

[40] Dorian Przetakiewicz, Stefan Wessel, and Francesco Parisen Toldin. *Boundary operator product expansion coefficients of the three-dimensional Ising universality class*. 2025. DOI: `10.48550/ARXIV.2502.14965`.

[41] Francesco Parisen Toldin, Abijith Krishnan, and Max A. Metlitski. "Universal finite-size scaling in the extraordinary-log boundary phase of three-dimensional O(N) model". In: *Physical Review Research* 7.2 (Apr. 2025), p. 023052. ISSN: 2643-1564. DOI: `10.1103/physrevresearch.7.023052`.

[42] Max Metlitski. "Boundary criticality of the O(N) model in d = 3 critically revisited". In: *SciPost Physics* 12.4 (Apr. 2022). ISSN: 2542-4653. DOI: `10.21468/scipostphys.12.4.131`.

[43] Michael Krech. "Casimir forces in binary liquid mixtures". In: *Physical Review E* 56.2 (Aug. 1997), pp. 1642–1659. ISSN: 1095-3787. DOI: `10.1103/physreve.56.1642`.

[44] Martin Hasenbusch. "The thermodynamic Casimir effect in the neighbourhood of the λ-transition: a Monte Carlo study of an improved three-dimensional lattice model". In: *Journal of Statistical Mechanics: Theory and Experiment* 2009.07 (July 2009), P07031. ISSN: 1742-5468. DOI: `10.1088/1742-5468/2009/07/p07031`.

[45] Jonathan Bergknoff. "The Critical Casimir Effect in Model Physical Systems". Appendix F. PhD thesis. University of California Los Angeles, 2012. URL: `https://jonathan.bergknoff.com/misc/bergknoff_dissertation.pdf`.

[46] Martin Hasenbusch. "Thermodynamic Casimir effect for films in the three-dimensional Ising universality class: Symmetry-breaking boundary conditions". In: *Physical Review B* 82.10 (Sept. 2010), p. 104425. ISSN: 1550-235X. DOI: `10.1103/physrevb.82.104425`.

Appendix A

Wolff Update Mistake

The question of how many Wolff single-cluster updates to perform per Monte Carlo step does not have an obvious answer. A natural target is to flip approximately $L_\perp L_\parallel^2$ spins per Monte Carlo step by analogy with Metropolis or Overrelaxation sweeps, but this is complicated because the mean Wolff cluster size varies strongly with temperature and system size. We initially adopted an approach that seemed to address this issue but contained a subtle conceptual error, as described below. The algorithmic idea was:

1. Start the Wolff routine and initialize a counter `site_counter = 0`.

2. Perform a Wolff update and increment `site_counter` by one each time a site is flipped.

3. Repeat Wolff updates until `site_counter` $\geq$ $L_\perp L_\parallel^2$.

4. Stop the Wolff routine.

Although this routine should meet the goal of flipping $L_\perp L_\parallel^2$ spins per step, comparisons of several observables with literature values revealed significant discrepancies. Switching instead to a fixed number of Wolff updates per step, for example $L_\perp$ cluster flips per step, restored agreement with reference data.

A plausible explanation for the failure of this update scheme is that detailed balance is subtly broken by the stopping rule. Detailed balance condition is only guaranteed if we pick a random site on the lattice and then perform a Wolff update. In the routine `site_counter` determines when the Wolff function stops, so the next Wolff update is dependent on all the previous updates performed in the

Wolff function. This introduces a bias in the size of the flipped clusters.

It would be interesting to investigate this further with a toy model. One could compare the Wolff cluster size distribution or directly check the detailed balance condition.